ABSTRACT

Title of thesis: IR THERMOGRAPHY AND IMAGE PHOTOPLETHYSMOGRAPHY : NON-CONTACT MEDICAL COUNTER MEASURE FOR INFECTION SCREENING

Yedukondala Narendra Dwith Chenna,
Master of Science, 2017

Thesis directed by: Professor Dr. Rama Chellappa
Department of Electrical and Computer Engineering

Screening based on non-contact infrared thermometers (NCITs) and Infrared Thermography (IRTG) shows promising results for mass fever screening. IRTGs were found to be powerful, quick and non-invasive methods to detect elevated temperatures. In the case of temperature measurement using IRTGs, regions medically adjacent to inner canthi are preferred sites for fever screening (IEC 80601-2-59:2008), which show good stability and correlation with body temperature. However, detection of canthi in thermal images is challenging due to the absence of features unlike visible images, which have sharp features that can be used for eye corner detection. We use registration of thermal images with visible light images (also called white-light images) to localize canthi regions in thermal images. We study the accuracy of such multi-modal image registration in the context of canthi detection and measure the feasibility of automatic canthi-based temperature measurement as an alternative to manual measurement.

The second part of thesis refers to the study of image photoplethysmography (IPPG), a cost-effective and flexible method for heart rate monitoring using videos recorded in ambient light. We use low-cost commercial grade video recording equipment (mobile camera/Digital camera) with an ambient light source. The study includes information about signal processing algorithms for estimating heart rate, relevant parameters, and comparison with standard techniques. Such low-cost, multi-purpose solutions for quick screening of subjects provides us with sensible and useful information on elevated body temperature and heart rate. Hence, these methods show promising results that enable mass fever screening as a possibility through temperature and heart rate monitoring, where low cost of installation and flexibility are important.

IR THERMOGRAPHY(IRTG) AND IMAGE PHOTOPLETHYSMOGRAPHY(IPPG) : NON-CONTACT MEDICAL COUNTER MEASURES FOR INFECTION SCREENING

by

Yedukondala Narendra Dwith Chenna

Thesis submitted to the Faculty of the Graduate School of the
University of Maryland, College Park in partial fulfillment
of the requirements for the degree of
Master of Science
2017

Advisory Committee:
Professor Dr. Rama Chellappa, Chair/Advisor
Professor Dr. Behtash Babadi
Dr. Quanzeng Wang

Acknowledgments

I owe my gratitude to all the people who have made this thesis possible and because of whom my graduate experience has been one that I will cherish forever.

First and foremost I'd like to thank my advisor, Professor Dr. Rama Chellappa and my mentor Dr. Quanzeng Wang for giving me an invaluable opportunity to work on challenging and extremely interesting projects. It has been a pleasure to work with and learn from such extraordinary people. I would also like to thank my co-advisor, Dr. Behtash Babadi for his support. My colleagues at the Optical Diagnostics laboratory at Food and Drug Administration (FDA) have enriched my graduate life in many ways and deserve special mention. Phejhman Ghassemi helped me throughout this study including assistance with setting up experiments/laboratory protocols setup and analysis of measurements. My interactions in team meetings with Joshua Pfefer and Jon Casamento have also been very fruitful.

I owe my deepest thanks to my family - my mother and father who have always stood by me and guided me through my career, and have pulled me through against impossible odds at times. Words cannot express the gratitude I owe them.

My friends here at University of Maryland have been a crucial factor, without whom the thesis would have been complete one month earlier. A special thanks goes to my friends here at College Park: Shankar, Koutilya, Goutham, Harsha, Harika, Abhinay, Surya, Navaneeth, Dayal , Raghu and others for making my graduate study enjoyable and memorable. Special thanks to Pallavi and Soumya for the reviews and edits during the initial draft. A special mention to my archrival, Deepika, for the

discussions on image registration, she was a great motivation and company.

I'd like to express my gratitude for their friendship and support. I would like to acknowledge financial support for Research Fellowship from Oak Ridge Institute for Science and Education (ORISE). It is impossible to remember all, and I apologize to those I've inadvertently left out.

Lastly, thank you all and thank God!

Table of Contents

List of Figures

List of Abbreviations

MMIR	Multi-Modal Image Registration
MI	Mutual Information
LC	Left Canthi
RC	Right Canthi
FH	Fore Head
SD	Standard Deviation
FFD	Free Form Deformation
IRTG	Infrared Thermograph
IPPG	Image Photoplethysmography
CC	Correlation Coefficient
SSD	Sum of Squared Difference
PPG	Photo Plethysmography
WHO	Word Health Organization
ICA	Independent Component Analysis
JADE	Joint Approximation Diagonalization of Eigen matrices

Chapter 1: Introduction

1.1 Overview

According to an estimate from World Health Organization (WHO), pandemic from viruses like Ebola, H5N1 bird flu could kill upto 100 million people [2]. Mitigating threat of such infectious pandemics may be possible through mass fever screening in public places such as airports, hospitals and border crossing points [7, 12]. Fever is one of the common diagnostic symptoms, which can be used to contain the epidemic through isolation of patients and medical care. In case of infectious diseases outbreak, a quick and efficient fever screening process is needed to identify infected patients. Early symptoms of infections can be detected through abnormalities in body temperature and heart rate. Conventional methods for measuring such human vital signals is invasive, time consuming and labor intensive [34, 44]. To enable mass fever screening we need devices/methods that are non-invasive, cost-effective, easy to install and be able to detect patients with fever [29]. Several studies [18] show that IRTGs enable a viable and non-invasive mass screening approach through detection of elevated temperatures. IRTGs have been used successfully as a tool for mass fever screening of SARS-2003 outbreak [29, 30]. Research in this area is necessary as epidemics like ebola, bird flu, zika are expected to hit 20 to 30 % of world's population.

International Organization for Standardization (ISO) meeting in 2005 at IEC-DIN Germany, discussed Standard Technical Reference [29, 40] to enable acceptance of infrared imaging in medical applications. Fever screening through IRTGs for human body temperature measurement requires identification of effective site for such measurement [30]. The regions medically adjacent to inner canthi are preferred sites for such fever screening based on temperature measurement (IEC/ISO 2008) [30]. This thesis tries to automate the process of temperature measurement using thermograms. Accurate localization of canthi regions is possible on visible light images, which are rich in features. Multi-modal image registration (MMIR) of thermal and visible images enables canthi localization in thermal images. Registration of multi-modal images from visible and IR face images is well studied in the literature on face recognition [21]. Accuracy of registration is studied in the context of canthi detection and the feasibility of automatic canthi-based temperature measurement as an alternative for manual measurement.

Similarly, recent techniques of IPPG investigate use of cost effective methods of heart rate monitoring using recorded video of the subject. This enables contact-free measurement of human vital signals at a distance from the subject, which is very appealing for mass fever screening application. These passive imaging methods enable long term monitoring of vital signals without any inconvenience to the patients. Studies include background information about signal processing algorithms for estimating heart rate, relevant parameters and comparison with standard techniques. Such low-cost, multi-purpose solutions for quick screening of subjects provide us with sensible and useful information about body temperature and heart rate. Abnormal-

ities in body temperature and heart rate are clear indicators of infection. These measurements can be used for screening such infected subjects. These recent developments in research show promising results that enable us to use consumer grade electronics as cost effective diagnostic tools for evaluation of body temperature or heart pulse rate through thermograms and recorded videos respectively. This thesis studies techniques of image registration to enable automatic IRTG-based temperature measurement and the feasibility of heart rate monitoring through commercial video recording equipment. The study evaluates influence of different parameters on performance of these methods along with experimental results.

1.2 Contributions of Thesis

This thesis explores different methods for registration of visible and IR face images to enable temperature measurement using inner canthi. Especially for a human face, which is non-rigid, affine models are limited in accuracy for registration. We implement a free form deformation (FFD)-based registration method to improve the registration accuracy after affine transformation. The improvement in registration accuracy using affine and deformable transformations is compared. We also evaluate the feasibility of registration-based automatic temperature measurement as an alternative to manual measurement. A complete implementation for registration of visible and IR images through affine and deformable transformations in MATLAB (The MathWorks. Inc.) is provided. In conclusion, we compare the manual canthi-based temperature measurement against automated image registration based

method.

Moreover, the study investigates the use of low-cost (mobile camera/Digital Camera) video recording equipment in ambient light for non-contact heart rate estimation. The recorded video using RGB color space with webcam/mobile camera shows heart rate pulsations in green channel which shows highest absorption. Changes in ambient light and automatic brightness adjustment in such video recording devices have significant influence on the underlining PPG signal. The study relies on manual segmentation to analyze different ROIs for heart rate estimation. We validate the performance characteristics through mean error, standard deviation of error, root mean square error (RMSE) along with Bland-Altman and correlation analysis. The thesis also studies the influence of different parameters like region of interest (ROI), window size for spectrum analysis and frame rate. This enables us to outline the requirements and their influence on heart rate estimation using IPPG.

1.3 Outline of Thesis

The thesis is organized as follows. Chapter 2 gives background information on IR thermography (IRTG) and image photoplethysmography (IPPG). Chapter 3 gives an introduction to image registration and its application in the context of IR Thermography. It discusses the implementation details of thermal to visible image registration and canthi temperature measurement along with results for measurement error analysis. Chapter 4 describes the experimental setup, input videos, overview of IPPG algorithm and results for heart rate estimation. Chapter 5 gives

conclusions drawn from experimental results.

Chapter 2: Theory

2.1 Infrared Thermography (IRTG)

IR cameras produce images to indicate temperature information from a surface. Thermography is a passive, non-contact imaging method that is cost-effective, quick and does not inflict any pain on the patient. The object surface temperature under observation governs the amount of IR radiation emitted from the surface. In case of fever screening, IR imaging is a non-invasive physiological test where the camera can be placed at a distance from the subject to be screened. Electrical signals generated by IR cameras are proportional to the IR radiations emitted from human skin [29], which are used to display temperature profile graphically. The image pattern indicates the inflammations (hot regions) and nerve dysfunction (cold regions). The observed temperature reading on human skin are below the typical body temperature of 37 $^{\circ}C$ due to heat evaporation, conduction and convection principles. The measured skin temperature, is a function of internal organ, heat properties of tissues and heat emissivity of skin. These features enable IR thermograms to be used for early identification or screening of individuals with elevated temperature as a first sign of infection [12]. In general, the setup for thermal imaging requires a stable indoor environment with stable ambient temperature (20 to

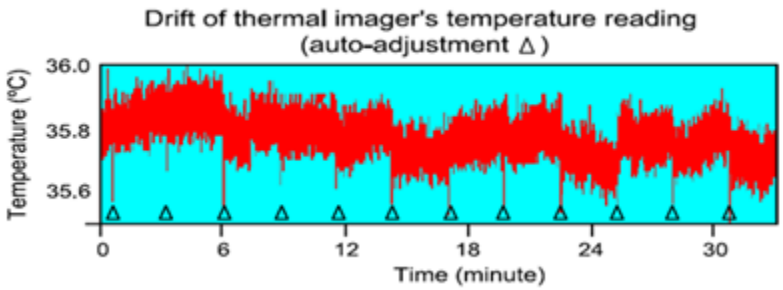

Figure 2.1: Thermal imaging temperature drift after auto-adjustment [30]

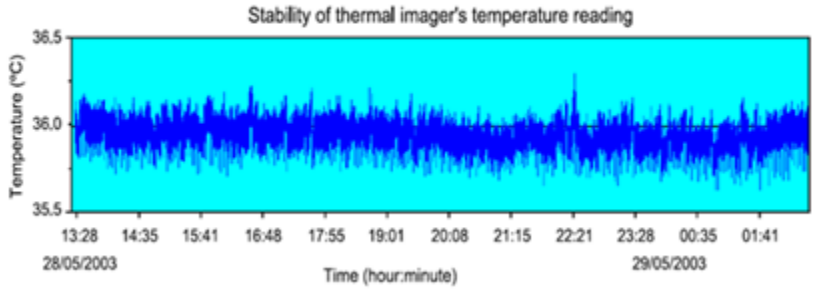

Figure 2.2: Temperature accuracy based on various sources of uncertainty [30]

25 $^{\circ}C$) and stability of +/- 1 $^{\circ}C$, with a relative humidity ranging from 40 % to 75 %. Based on the type of IR imaging, they have different degrees of temperature drift depending on self-correlation (Fig.2.1), uniformity within field of view, minimum detectable temperature difference, error and stability of threshold temperature (Fig.2.2), distance effect and detector sizes. An external black-body maintained at given temperature is used as a reference to correct the thermograph for any drift in temperature sensitivity. This enables satisfactory repeatability of the temperature measurement. The temperature readings from the camera are calibrated based on the measurement from the black body used as a temperature reference.

Many other factors that influence temperature measurement include : parameters of IR imaging system, variation in operating environment and screened subjects. These variations might lead to false-negative readings which will strongly undermine the effectiveness of the screening process. Hence, a reliable and scientific method for accurately estimating the body temperature is essential for successful implementation of such mass fever screening methods. A recent research [30], studied different regions on IR face images that show good correlation with body temperature. The IEC 80601-2-59:2008 international standard indicates that the canthi regions (Fig.2.3) provide accurate estimates of core body temperature, since the canthi regions are supplied by the internal carotid artery and are less susceptible to external environmental changes. Anatomically these regions are adjacent to inner corner of the eye and vary in size from subject to subject. Therefore, rapid, automated identification of the canthi regions (Fig.2.4) within facial IR images may greatly facilitate fever screening. Automatic localization of canthi in thermal images is achieved through MMIR of thermal and visible images, followed by fiducial point detection [4] in visible face images to localize the canthi regions. The canthi regions on thermal face images are used to measure temperature and compare its feasibility with manually obtained temperature measurement.

2.2 Image Photoplethysmography (IPPG)

Plethysmography steams from Greek work plethysmos meaning variations in size owing to blood circulation. Conventional plethysmography measures pulsativ-

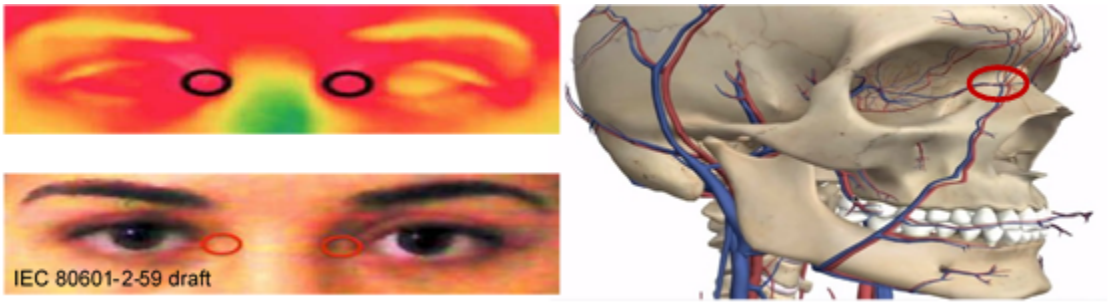

Figure 2.3: Canthi regions for fever screening (IEC 80601-2-59:2008) [1]

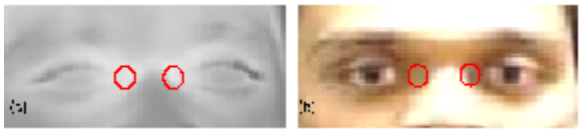

Figure 2.4: The canthi regions for fever screening (a: an IR image; b: a white-light image) [9]

ity in tissue volume and blood profusion directly through strain gauge. The gold standard currently for measurement of cardiac pulses is through electrocardiogram (ECG). It requires patient to wear adhesive gel patches or chest straps, which can cause skin irritation or discomfort. The commercially available pulse-oximetry, which are generally attached to fingers or ear lobes are inconvenient for subjects and can cause pain over long duration. Availability of a remote and non-contact based monitoring or screening systems for cardiovascular activity is an interesting prospect for primary health care and surveillance. Pavlidis *et. al.* [17] demonstrated an approach for measuring of physiological parameters through face and thermal videos. Photo Plethysmography (PPG) is a low-cost and non-invasive means of sensing cardiovascular pulse by measuring the variation in transmitted or reflected

light through tissues [38]. Such methods may not provide the details of cardiac electrical conduction as in ECG, but they give useful information on heart pulse rate by acquiring short duration videos in an unobstructed and comfortable manner. Typically, conventional PPG has a dedicated light source, which can be broadly classified into two types: Transmission mode PPG and Reflectance mode PPG. Transmission mode PPG measures how light is obstructed and absorbed through tissues using an LED light source on one side and a photodetector on the other. Reflectance mode PPG has the LED and photodetector on the same side and studies the amount of light reflected from a tissue surface. The underlying PPG signal in such plethysmographs is a complex function of physiological parameters, measurement methodology and physical properties of sensor.

Non-contact image PPG (IPPG), is a type of reflectance mode PPG which uses video recordings with ambient light sources. It is an active field of research, offering insights into implementation of non-invasive human vital sign monitoring [42]. The basic principle of IPPG relies on interaction of ambient light with biological tissues. Similar to conventional PPG signals, it is a complex function of physiological parameters, acquisition system and the properties of light scattering. The light interactions with biological tissues results in intensity modulation in the recorded video which is synchronous with heart beat. There are many intrinsic components that influence these fluctuation in intensities like blood volume, blood-vessel-wall movement and the orientation of the red blood cells. One of the main contributors of such variations is blood flow and volumetric change in blood-vessel due to movement of blood stream. The absorption spectrum within color spectrum for

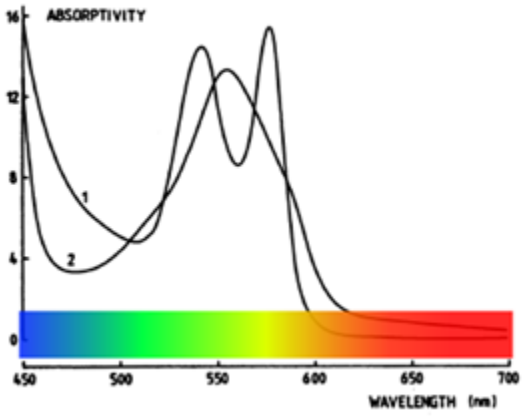

Figure 2.5: Absorption spectrum of Hemoglobin within 450 nm to 700 nm wavelength range [49]

wavelength span of 450-700 nm for (1) oxyhemoglobin (HbO2) and (2) deoxygenated hemoglobin (Hb) as shown in Fig. 2.5. The green light shows peak absorption and red shows the lowest absorption, which is validated based on observations from experimental results. Such non-invasive assessements of cardiovascular activity are useful in surveillance to estimated abnormalities in heart pulse rate.

Chapter 3: IR Thermography (IRTG)

3.1 Image Registration

Image registration is fundamental to a wide range of applications in medical imaging. Image registration can be modeled as a transformation that defines a spatial correspondence between two images. It is the process of spatially aligning two or more images captured using various modalities and at different viewing angles and time instants. Registration methods can be broadly classified as follows [23]:

I. Nature of Registration : (i) Extrinsic and

: (ii) Intrinsic

II. Image Modality : (i) Uni-modal and

: (ii) Multi-modal

III. Similarity Metric : (i) Landmark based and

: (ii) Intensity based

IV. Transformation Model : (i) Rigid

: (ii) Affine and

: (iii) Deformable

3.1.1 Nature of Registration

Based on the nature of registration, registration methods can be classified into extrinsic and intrinsic methods. Extrinsic methods use artificial objects, which are either placed within the field of view or attached to the subject, while capturing the image. These objects are designed to be easily detectable in two or more images (which are) to be registered and are used for estimating the spatial transformation for registration. Extrinsic object based registrations are relatively fast and enable automation. However, these methods are limited due to constraints on the provision of such objects under different conditions, additional cost and advanced planning before image capture. This model does not use any information from the subject and is mostly limited to rigid transformation.

Intrinsic methods use information from a subject image, the transformation is based on identifiable features from the images to be registered. Intrinsic methods can be broadly classified into (a) Landmark-based and (b) Intensity-based approaches. Landmark-based registration uses features points identified in different images and determines the transformation based on these feature points, which are easy to locate by the user or automated algorithm. Landmark-based methods are generally used to define rigid or affine transformations. If the number of feature points is large enough more complex deformable transformations can be estimated. The search for optimum transformation is simplified due to sparse landmark points, which greatly speeds up the registration process. Nonetheless, it usually requires user interaction for the landmark selection, which limits its applications. Intensity-

based methods use the intensity values of pixels. These methods enable flexibility for applications with similar or different modality images and can be adapted to most type of transformations. However, these methods are limited in application due to computational complexity of registration.

3.1.2 Image Modality

The registration method can be classified into two types based on modality of images involved : (a) mono-modal image registration and (b) Uni-modal image registration (MMIR) [24]. In uni-modal registration, the images to be registered have been acquired using similar sensors, but from different view points, or times or scales. Uni-modal registration is quite widely used in growth monitoring, comparison, subtraction imaging, and many other applications. In case of MMIR, the images to be registered are obtained using different sensors. MMIR of images provides complementary information, which uses comparison of spatial points for useful information about infection or disease.

3.1.3 Similarity Metric

Similarity metric is used to define a qualitative metric for alignment of the images to be registered. The registration algorithm tries to minimize/maximize the similarity metric to achieve spatial alignment of images. Similarity Metric is crucial in the image registration algorithm. It determines the accuracy, robustness and flexibility of registration algorithms. These measures can be broadly classified

into: landmark-based and intensity-based measures. Landmark-based methods use unique landmarks in both the reference and moving images, which can be used to estimate the transformations. Landmarks can provide a basis for Rigid/affine transformation. Alternative includes extraction of feature points in one image and matching them in another image. Intensity-based methods work directly with pixel intensity level. However, intensities obtained with different modalities do not show a linear relation. Other methods that do not rely just on intensity value, but try to model the correlation are better suited for MMIR. Intensity based metrics widely used in MMIR for medical images, include Sum of Squared Difference (SSD) [24], Normalized Cross Correlation (NCC) [24], Correlation Ratio (RC) [24] and Mutual Information (MI) [24]. In this section we will briefly discuss SSD, NCC and MI methods, which are quite widely used in medical image registration. Simplest measure for the similarity of images is based on the SSD between images I_{reg} and I_{mov} with transformation $T(x, y)$ given by:

$$I_{SSD} = \sum [I_{mov}(T(x, y)) - I_{reg}(x, y)]^2 \tag{3.1}$$

This measure is used for images with similar modality, which is optimal if images with white Gaussian noise are aligned. A more general approach assumes a linear relationship between image intensities. In such a case similarity between images I_{reg} and I_{mov} can be expressed using NCC

$$I_{NCC} = \frac{\sum (I_{reg}(x, y) - \mu_{ref})(I_{mov}(T(x, y) - \mu_{mov})}{\sqrt{\sum (I_{reg}(x, y) - \mu_{reg})^2 \sum (I_{mov}(T(x, y)) - \mu_{mov})}} \tag{3.2}$$

Where the images are corrected with μ_{reg} and μ_{mov} representing mean image intensity. This metric is more flexible than SSD, nevertheless it is restricted to mono-modal registration. Mutual Information as a metric for image registration was first proposed by Woods *et al* . [48]. In case of MMIR, regions with certain intensity level in an image would correspond to similar regions in another image that contain a similar intensity level distribution (maybe of different value). Ideally, the correspondence between these intensity level distribution might not change significantly across different images. Hill *et al.* [13] proposed registration by constructing a joint histogram, which is a two-dimensional plot showing combinations of grey values as shown in Fig.3.1. Location (i, j) in the joint histogram corresponds to a count of the values with intensity 'i' in the first image and intensity 'j' in the second image. The joint histogram shows increased dispersion as the misalignment of images increases. Shannon entropy (also referred to as entropy) [24] is used as a registration metric to measure dispersion in the joint histogram. Entropy of a discrete random variable X_i with probability distribution function p_i is given by [24]:

$$H(X) = -\sum p_i(log_2(p_i)) \tag{3.3}$$

Entropy does not depend on the value of a random variable, but depends on the distribution of the random variable. This definition of entropy can be extended to images, where the probability distribution function is constructed using the histogram distribution of pixel values in the image. Entropy of a joint histogram decreases with better alignment of the images as shown in Fig.3.1. Define MI as

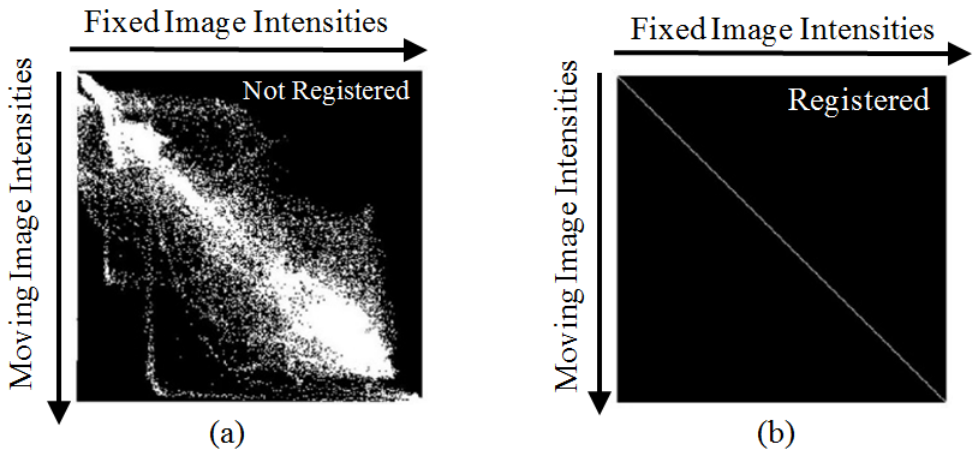

Figure 3.1: Joint histograms for measuring registration accuracy using Mutual Information (a) Mis-aligned Images (b) Ideally Registered Images

I_{MI} based on the entropy of two input images A and B, which relates to the joint histogram entropy as follows:

$$I_{MI} = H(A) + H(B) - H(A, B) \tag{3.4}$$

Where $H(A)$, $H(B)$ and $H(A, B)$ are the entropy's of image A, image B and the joint histogram, respectively. The above equation relates the minimization of the joint histogram to the maximization of MI. Hence, the problem of registration is converted into an optimization problem that tries to maximize the MI using different transformations.

3.1.4 Transformation Model

Transformation Model is one of the key problems in image registration. The transformation model used in registration defines how the coordinates of two images are related. These models can be broadly classified into global and local transformation models. Global transformation is applied to the whole image, whereas local transformations are applied to each pixel or group of pixels in the image. Global transformations are quite widely used because of their simplicity in estimating few parameters. Simple translation and rotation motion of a planar object can be defined as a rigid transform. Affine transformation allows scaling and shear in addition to the rigid transform. Local transformations are used to model registration of non-planar surfaces, where the motion or registration cannot be modeled by global parameters. A generic transformation can be defined as a combination of global and local transformations:

$$T(x, y) = T_{global}(x, y) + T_{local}(x, y) \tag{3.5}$$

Consider two images I_{ref} and I_{mov}, which represent reference and moving images, respectively. The transformation T is applied on the moving image and measures the similarity metric. The optimization process tries to minimize/maximize the similarity metric over all possible parameters of the transformation. Let I_{reg} denote the registered image. The goal is to find T (or equivalently its inverse) which provides a mapping from I_{mov} to I_{reg}.

The relation between I_{reg} and I_{mov} can be defined as follows:

$$I_{reg}(T(x,y)) = I_{mov}(x,y) \tag{3.6}$$

Where T is a transformation defined by a global and a local transformation. The goal is to estimate T, that maximizes/minimizes the similarity metric. Transformation (T) is defined on the image coordinates of the moving image I_{mov} transforming it to I_{reg}, which try to match the I_{ref} image coordinates. The global transformation (T_{global}) is the product of geometric transformations, which includes translation, rotation, scaling and skew as shown below:

$$T_{global} = \begin{bmatrix} 1 & 0 & t_x \\ 0 & 1 & t_y \\ 0 & 0 & 1 \end{bmatrix} \begin{bmatrix} \alpha & -\beta & 0 \\ \beta & \alpha & 0 \\ 0 & 0 & 1 \end{bmatrix} \begin{bmatrix} 1 & k & 0 \\ 0 & 1 & 0 \\ 0 & 0 & 1 \end{bmatrix} \begin{bmatrix} S_x & 0 & 0 \\ 0 & S_y & 0 \\ 0 & 0 & 1 \end{bmatrix} \tag{3.7}$$

$$t_x, t_y = Translation\ of\ the\ image\ in\ the\ x\ and\ y\ direction$$

$$\theta = angle\ measured\ in\ the\ counter\ clockwise\ direction\ from\ the\ x-axis,\ (\alpha = cos(\theta),\ \beta = sin(\theta))$$

$$k = shear\ factor\ along\ the\ x-axis$$

$$S_x, S_y = change\ in\ scale\ in\ the\ x\ and\ y\ direction$$

A Local transformation improves the registration accuracy for non-planar surfaces. However, the large number of parameters to be estimated and high computational complexity limits its application. Deformable registration is used to model

non-planar transformations locally displace a moving image I_{mov} as shown in eq.3.8. These registration models offer higher degrees of freedom to represent the transformation. This enables modelling of local deformation more accurately resulting in high accuracy registration. Free Form Deformations (FFDs) are well studied non-rigid models used to describe more general deformations for each pixel or a group of pixels with high degrees of freedom and with smoothness constraints in the deformation. FFDs can be broadly classified into parametric and non-parametric transformations. The parametric transformations are defined on a coarse grid of control points, where the transformation is parametrized by basis functions. In contrast, non-parametric transformations have a dense set of displacement vectors associated with every pixel in the image. Such algorithms are used to describe more general deformations for each pixel with a high degrees of freedom, along with smoothness constraints. In case of parametric transforms, where T is expressed as the displacement field (u, v) on a coarse grid of control points, as in eq.3.8. The transformations are required to be smooth and invertible. In case of non-parametric FFDs like demons algorithm, it includes an additional smoothness constraint on transformation using the weighted Gaussian function. These transformations require a great deal of computation time, which can be improved through numerical algorithms and coarse-to-fine registration strategy. The parametrized and non-parametrized algorithms can be defined as displacement vectors for moving image $I_{mov}(x, y)$ with a transformation as follows.

$$T(x, y) = (x + f(u),\ y + f(v)), \tag{3.8}$$

where u and v are vertical and horizontal displacement fields, f is the basis function used to define the transformation. Given a pair of images I_{ref} and I_{mov} which are used to simultaneously recover u and v. A weighted blend of these displacement field from neighborhood is used to determine the displacement of a pixel in the image. The blending weights are determined by a weighted Gaussian function and cubic B-splines for demons algorithm and Spline registration, respectively. The displacement vectors in case of Cubic B-spline registration at each pixel is defined as a combination of B-spline basis functions, which themselves provide smoothness constraints on the transformation.

3.1.4.1 Demons Registration

Demons Algorithm [43] proposed deformable registration as a diffusion process, which introduces entities called Demons that exerts forces according to the local characteristics of the images. These forces were inspired from optical flow equations [14]. It can be considered as a type of viscous fluid model-based registration. The basic idea of the Demons algorithm for deformable registration is that the reference image acts as a local displacement vectors that moves the pixels in the moving image to match the reference image. During each iteration, the moving image is transformed using the moving vector $dV = (dx, dy)$ for each pixel as shown in eq. 3.8 [11]:

$$dV^{(n+1)} = \frac{(I_{mov}^{(n)} - I_{ref}^{(0)})(\nabla I_{ref}^{(0)})}{(I_{mov}^{(n)} - I_{ref}^{(0)}) + |\nabla I_{ref}^{(0)}|} \tag{3.9}$$

Where $I_{ref}^{(n)}$ and $I_{mov}^{(n)}$ are the intensities of reference and moving images, respectively, at the n^{th} iteration. $I_{ref}^{(0)}$ and $I_{mov}^{(0)}$ represent the original reference and moving images, respectively. A Gaussian filter is used to smooth the displacement fields, which suppresses noise and preserves the geometric continuity of the deformed image. This algorithm can be efficiently implemented using using convolution operation, which enables its application to registration problems which require high dimensions. The gradient of the reference image $\nabla I_{ref}^{(0)}$ is computed only once for all the iterations. Moreover, the Demons algorithm assumes that the displacement vector is reasonably small or local. However, in real clinical cases, such an assumption may be violated. To reduce the magnitude of displacement vectors, the multi-scale approach is used, where both reference and moving images are down-sampled to low resolution images using Gaussian pyramid scaling. The displacement fields at each stage are up-sampled from a low resolution scale to a higher resolution scale. This provides a significant computational advantage for large image sizes. However, the conventional Demons algorithm is applicable only to uni-modal image registration [35, 50]. In this study, the edge maps for IR and visible images generated using a canny edge detector are used for estimating FFD registration using Demons algorithm. These edge maps emphasize on the contour edges of face and eyes, which show a good similarity between thermal IR and visible images [22]. The contours in eye regions are used to predict the free-form transformation used for non-rigid

registration. Iterative optimization method uses an effective stopping criteria, a tolerance criterion that stops the iterations if the SSD in intensity value increases with each iteration and also if the decrease in the similarity metric for each iteration is within a convergence tolerance.

3.1.4.2 Spline Registration

Spline-based registration models are among the most common and important transformation models used for deformable registration in medical imaging. Spline-based registration algorithms use coarse grid of control points from the moving image and a spline basis function that defines the transformation in the neighborhood of these points. The spline based registration can be divided into two types : (a) thin-plate splines and (b) B-spline. Thin-plate splines have a global influence on the transformation. In contrast, B-splines are only defined in the neighborhood of control points. Any perturbation in control points influences points within the neighborhood of that point. This makes B-spline based registration a computationally efficient tool for deformable registration. Cubic B-spline based FFDs deform an object by manipulating the underlying mesh of control points. The vector fields (u_i,v_i), represent the dense displacement fields estimated as two dimensional splines controlled by a small number of control points (U_j,V_j) highlighted in red as shown in Fig.3.2. The spline imposes an implicit smoothness on the motion fields, eliminating the need for additional smoothness constraints, in many instances. To define a spline based FFD, defined on mesh of n_x by n_y control points with uniform spacing.

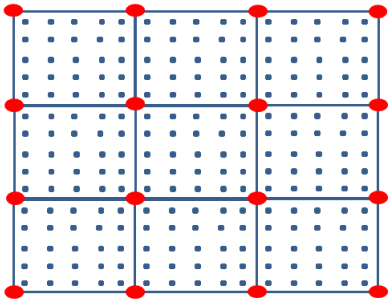

Figure 3.2: B-spline mesh grid control points

The u_i and v_i defines the displacement vectors at each pixel given by:

$$u_i = u(x_i, y_i) = \sum U_j B_j(x_i, y_i) = \sum U_j w_{ij} \tag{3.10}$$

Where $B_j(x_i, y_i)$ are called basis functions and are non-zero over a small interval. $w_{ij} = B_j(x_i, y_i)$ weights that are used to emphasize that (u_i, v_i) are known linear combination of (U_j, V_j) control points.

Implementation of B-spline makes the spline control grid on a regular grid of sampling points $(X_j, Y_j) = (mx_i, my_i)$, so that each set of mxm pixels corresponds to a single spline patch. The basis functions are spatially shifted versions i.e. $B_j(x, y) = B(\frac{(x-X_j)}{m}, \frac{(y-Y_j)}{m})$. Fig.3.3 visualizes four different types of basis functions:

I. Block : B(x,y)=1 on [0,1][0,1]

II. Linear : (1-x-y) on [0,1][0,1]

: (x+1) on [-1,0][0,1]

: (y+1) on [0,1][-1,0]

III. Quadratic : $B_2(x)B_2(y)$ on [-1,1][-1,1]

where $B_2(x)$, $B_2(y)$ are second order (quadratic) B-Spline

IV. Cubic : $B_3(x)B_3(y)$ on [-1,1][-1,1]

where $B_3(x)$, $B_3(y)$ are third order (cubic) B-Spline

B-splines are locally controlled, which makes them computationally efficient. The basis functions of cubic B-spline have a limited support, changing the control point affects the transformation only in the local neighborhood of control point. The control points' resolution determines the number of degrees of freedom and consequently the computational complexity. A large spacing between control points allows modeling of global non-rigid deformations, while a small spacing between control points allows modeling of highly local deformations. In the multi-scale approach, the spacing between control points decreases from a lower resolution to higher resolution, which increases the resolution of control mesh. At each level of resolution, the control mesh and associated spline-based FFD defines a local transformation. To avoid the overhead of calculating several B-spline coefficients separately, the local transformation defined by a single B-sline whose control point mesh is progressively refined. The control point mesh at level L is refined by inserting new control points to create the control point mesh at level L+1. The number of horizontal and vertical control points double every step. The spline-based FFD transformation can

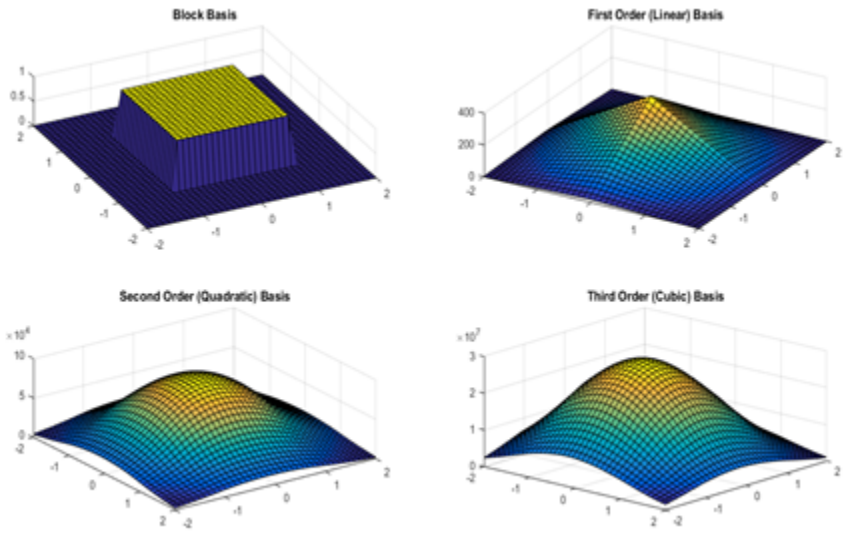

Figure 3.3: BSpline basis functions

be smoothed by introducing a penalty regularization term. The MIRT [3] tool used for cubic B-spline registration uses curvature regularization based on discrete cosine transformation (DCT) [10], to yield a stable and fast implementation.

3.1.4.3 Interpolation

At each iteration of registration, the optimizer determines the parameter of the transformation (T) that will be applied to the moving image, also called image warping. Image warping is defined as the process of transforming the moving image using the estimated transformation. Irrespective of the type of transformation, rigid or deformable, interpolation is an important step in registration. The transformed image is used to calculate the similarity metric for comparison between the moving and fixed images.

The transformation gives information about the pixel movement through the transformation matrix or displacement field vectors [26]. Once the transformation (T) is estimated, the transformed image I_{reg} defined as:

$$I_{reg}(T(x, y)) = I_{mov}(x, y) \tag{3.11}$$

This is referred to as 'forward warping' i.e. the location of a pixel in the new image is calculated from the previous image. When such transformations are applied to a moving image, the pixel values in the moving image might not map to grid points in the transformed image as shown in Fig 3.4. This might lead to some pixels being assigned multiple values and some other pixels not assigned any value. Backward warping is used to avoid such conditions, where for every pixel in the new image an inverse transformation (T^{-1}) maps it to the location in the original image as shown Fig .3.5. In many cases it is acceptable to have a simple approximation of the inverse transformation as:

$$T^{-1}(x) = T(x, y) - (u(x, y), v(x, y)) \tag{3.12}$$

In case of pixels transformed to non-grid locations from inverse transformation, the pixel intensity value can be computed using traditional interpolation techniques on the original image. The most commonly used interpolation methods include the nearest neighbor, linear interpolation, bi-linear interpolation and B-spline interpolation [19]. The simplest interpolation method is the nearest neighbor interpolation, which finds a pixel nearest in neighbor grid position. Linear interpolation assumes

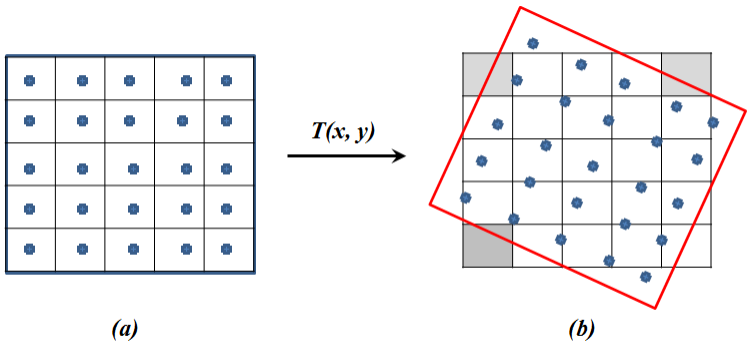

Figure 3.4: Forward warping method for spatial transformation

that the intensity variation is linear within grid positions. Higher order interpolation methods, which are more accurate require more computations and consequently are slower. Recent developments also include interpolation methods recommend the use of use of higher order basis functions [19]. The interpolation methods need to be applied at every iteration of the registration process which directly influences the computational complexity of registration. It also influences the similarity metric which affects the optimization process. Hence, the selection of the interpolation scheme is a trade-off between computational complexity and its effectiveness in estimation of pixel values.

3.1.5 Optimization

An optimization method tries to optimize the specified similarity metric over the search space of possible parameters for the transformation model. An effective optimizer is one that reliably and quickly finds the best possible transformation.

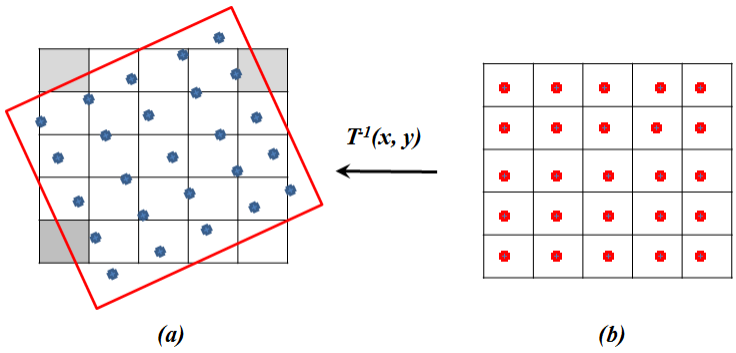

Figure 3.5: Backward warping method for spatial transformation

Selection of an optimizer depends on the transformation model, the constraint that would be applicable and the numerical analysis. Most of these optimization algorithms for registration can be expressed as follows:

$$a_k = argmin\ S(\mu_k + ad_k) \tag{3.13}$$

where S is the similarity metric/cost function for image registration, μ_k are the parameters of registration, a_k is the gain factor that decides the magnitude of the step size and d_k defines the search direction. Optimization methods for image registration vary mainly on the basis of how the gain factor a_k and the search direction d_k are calculated.

In deformable registration applications, the optimizer is more complicated, as non-rigid transformation models have high degrees of freedom and thus has more parameters. The selection of the optimization method depends on the application, transformation model, time constraint and the required accuracy of registration.

Many of these registration algorithms are amenable to gradient descent-based optimization schemes [31] using existing numerical solvers [31], in that they seek to choose a set of parameters to maximize (or minimize) a cost function based on the gradient of cost function. The gradient descent method moves the solution towards the negative (or positive) direction of gradient to minimize (or maximize) the similarity metric.

$$\mu_{k+1} = \mu_k + a_k(g(\mu_k)) \tag{3.14}$$

$g(\mu_k)$ is the derivative of cost function evaluated at the current position μ_k. The similarity metric must be differentiable to enable derivative based optimization methods, which iteratively select parameters such that the similarity metric is minimized (or maximized). Good initial estimates are necessary to avoid convergence on a local extrema. To guide the convergence towards the global minimum, the implementation uses a multi-scale strategy using Gaussian image pyramid [20]. The current implementation used gradient decent based optimizer in MATLAB [31] for rigid and deformable registration.

3.2 Implementation: Thermal and Visible Image Registration

To implement automated temperature measurement using canthi regions, accurate IR and visible image registration is essential for localization of the canthi regions is essential. The two-step registration strategy with coarse and fine registrations is illustrated in Fig. 3.6. Coarse registration is used for the initial alignment

Figure 3.6: Block diagram of the two-step registration strategy

of images and detecting the region of interest (ROI). Fine registration is used to improve the registration accuracy to enable accurate detection of the canthi regions within the ROI. The scheme for proposed algorithms is presented in Fig. 3.6.

3.2.1 Coarse Registration

Coarse registration based on MI is used to define the affine transformation followed by face detection. The face detection algorithm is based on work by Viola and Jones [46], a cascade boosted classifier uses Haar-like digital image features trained with positive and negative examples. The pre-trained frontal face classifier available with MATLAB computer vision library is used to obtain the face location [32] and size of face region. Coarse registration is used for selecting the ROI around the face after registration and is primarily based on MI. Coarse registration is defined on affine transformation. The coarse registration algorithm is implemented in MATLAB using Mattes MI algorithm [24]. In this algorithm, the marginal and joint probability density functions (PDF) are evaluated at discrete position using samples of pixel intensities. The regular step gradient descent optimizer [31] is used for implementation of this algorithm. Fig.3.7 shows the block level diagram for image registration of IR and visible images.

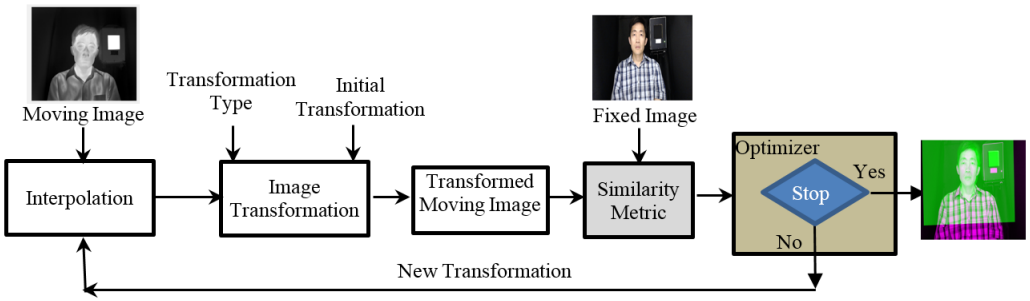

Figure 3.7: Block Diagram of Image Registration

3.2.2 Fine Registration

Fine registration is used to improve the registration accuracy of IR and visible images for better localization of the canthi regions. Unlike the affine transformation used for coarse registration, the fine registration uses FFDs with displacement vectors for each pixel in the image. To model local deformations of the face which are difficult to describe via affine transformations, an FFD model based on non-parametrized (Demons) and parametrized models (Cubic B-spline) is used. The FFDs based on deformable registration is widely used in medical imaging. The edge maps generated with Canny edge detector [22], which contains the contours which are consistent in both visible and IR images, are used to estimate FFD. This is used to improve the accuracy of coarse transform. The results of registration on pair of IR and visible images are studied to get an understanding of improvement in registration. The input IR and visible images are shown in Fig. 3.8.

Fig.3.9. shows the respective edge maps extracted from the canny edge detector. Fig.3.10. shows the registration results on the edge map pairs after Affine

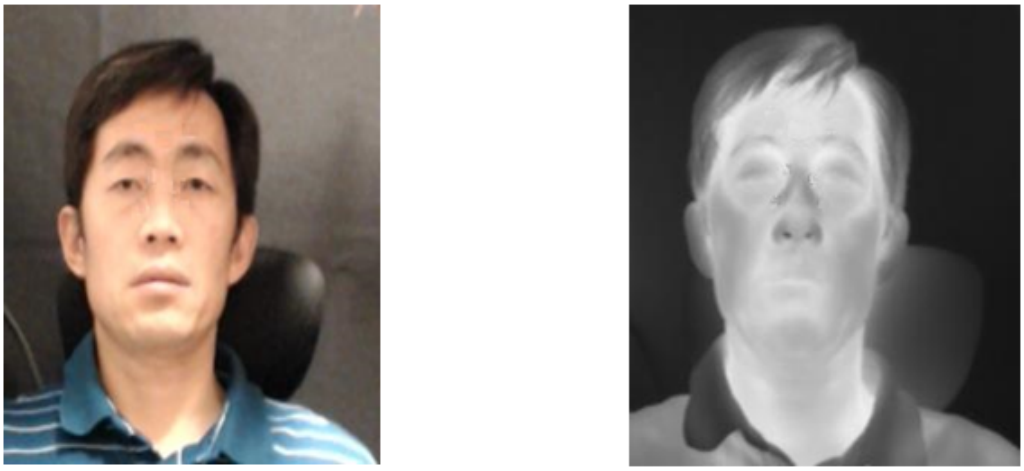

Figure 3.8: Input IR and visible Images after coarse registration and ROI Selection

and Affine + Demons algorithm. The results show that prominent edge features like eyes, nose and mouth show better alignment in fine registration (Affine + Demons Algorithms) compared to coarse registration (Affine Registration).

Fig.3.11. shows image registration results viewed through superimposed checkerboard pattern of visible (gray scale) and IR images. It can be observed that the eyes and nose are not accurately aligned in case of affine transformation. In contrast, the registration after Demons algorithms has much better alignment. This demonstrates that applying non-rigid registration improves accurate matching of face images compared to using only affine transforms. Qualitative metric for measuring the improvement in registration is discussed in the next section.

Figure 3.9: Edge maps for IR and visible Images after ROI Selection

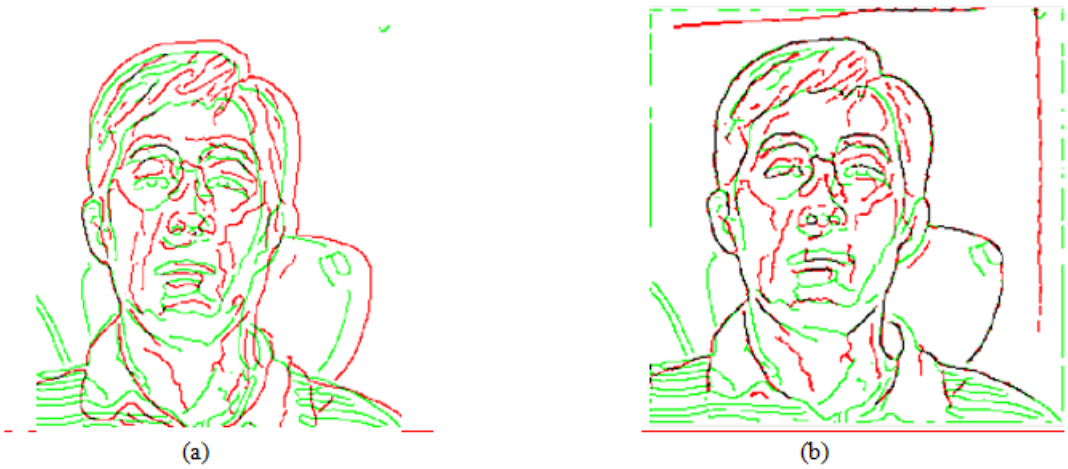

Figure 3.10: Image Registration using edge maps after: (a) Affine (b) Demons registration

Algorithm 1 Demons Algorithm

1: Initialize the displacement vector with zeros

2: Scale the input images to current pyramid level

3: Interpolate the vector fields from earlier pyramid level and transform the I_{mov} moving image

4: Calculate gradient of reference image at current pyramid level $\nabla\ I_{ref}^{(0)}$

5: Calculate the I_{diff} difference image after transformation of moving image

$$I_{diff} = (I_{ref} - I_{mov})$$

6: Update the displacement fields as:

$$\mathrm{dV}^{(n+1)} = \frac{(I_{mov}^{(n)} - I_{ref}^{(0)})(\nabla I_{ref}^{(0)})}{(I_{mov}^{(n)} - I_{ref}^{(0)}) + ||\nabla I_{ref}^{(0)}}$$

7: Smooth the displacement fields using Gaussian Filter

$$T(x, y) = dV^{(n+1)} * G(x, y)$$

8: Calculate SSD, repeat Step 2-7 until :

$$\mathrm{I}_{SSD} = \sum [I_{mov}(T(x, y)) - I_{ref}(x, y)]^2$$

(a) SSD increases over iteration

(b) SSD decreases less than a convergence threshold

(c) Maximum number of iterations reached

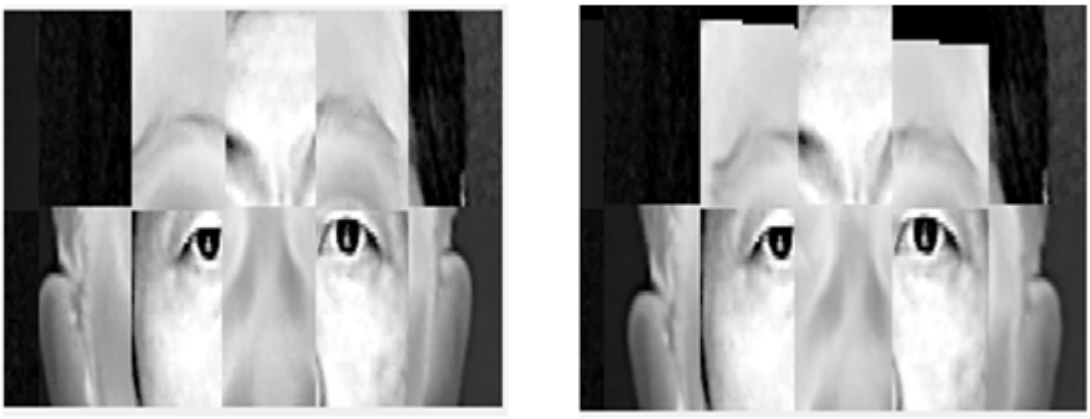

Figure 3.11: Registered images using checkered view (a: coarse registration; b: fine registration)

3.3 Results and Analysis

3.3.1 Registration Accuracy

The images of volunteers were captured using three different cameras Fig. 3.12. shows i) an IR camera from FLIR Systems Inc. (IRT1), ii) an IR camera from Infrared Cameras Inc. (IRT2), and iii) a visible camera from Logitech. These images are used as input images for image registration. Circular aluminum foils with diameter of 7 mm were attached to different locations around the canthi regions of the volunteer as landmarks. The captures IR and visible images were used as the input images for image registration. The landmarks and their correspondence between image pairs were manually selected from the input images as control points as shown in Fig. 3.13. After image registration, the Euclidean distance between each pair of control points in IR and visible images was calculated as a qualitative

Figure 3.12: Images from three cameras (a: IRT1; b: IRT2; c: visible camera)

performance metric. The average matching error of the coarse registration is around 4.92, 2.75 and 2.59 pixels on three individuals. It improves significantly to average error of about 2.01, 2.06 and 1.60 pixels respectively for fine registration as recorded in Table 1. The scale factor of image is measured to be 1.2 mm/pixel. The absolute mean error of registration in canthi region, after multiplication with scale factor of 1.2 mm/pixel, is ± 2.26 mm in localization of canthi region. This shows promising results for automated and accurate localization of canthi region for temperature measurement in fever screening. We evaluated the uncertainty in manual selection by repeating the experiment on 30 manual selections for the same image. These give us a statistical measure of uncertainty (standard deviation) in manual selection to be ± 0.57 mm (SD).

This study tries to give a quantitative comparison of the implementation for registration of IR and visible images. The recall parameter [21], computed on all landmark pairs of a face, where recall/true positive is defined as the ratio of true positive correspondences to the ground truth. The true positive correspondence is

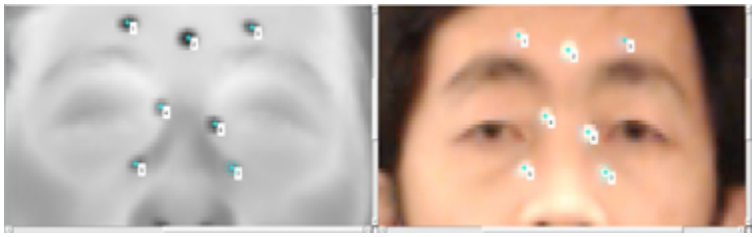

Figure 3.13: Control point selection for registration evaluation (a: IR image; b: visible image)

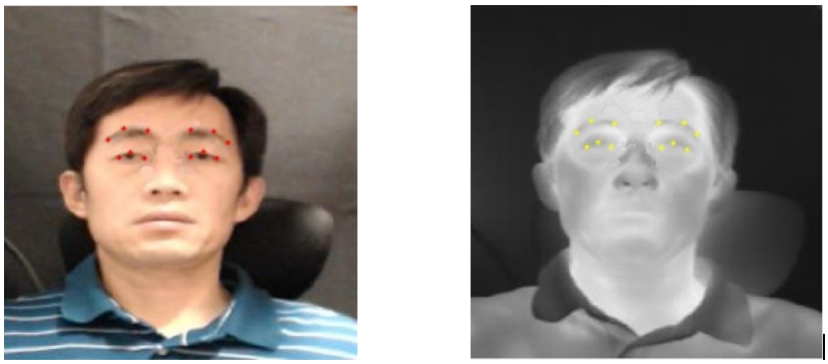

Figure 3.14: Control point selection in eye region for registration evaluation (a: IR image; b: visible image)

Table 3.1: Registration Matching Error- Landmarks (in pixels)

Methods/Algorithm (Similarity Metric)	Sub. No. 1	Sub. No. 2	Sub. No. 3
Affine (MI)	4.92	2.75	2.59
Affine (MI) + Demons (SSD)	2.01	2.06	1.60
Affine (MI) + Cubic B-spline (SSD)	2.84	2.55	2.43
Affine (MI) + Cubic B-spline (SSD)	3.15	2.57	2.35

counted when the pair falls within a given accuracy threshold in terms of pairwise distance i.e. Euclidean distance between a landmark in the warped model point set and the corresponding landmark in the data point set. The landmark selection and point correspondence between image pairs is manually constructed. The point correspondence on contours around eye region like eyes corners, eye brows and pupil as ground truth are identifiable in both IR and visible images as shown in Fig.3.13. In addition to Affine, Demons algorithm, we use cubic-BSpline registration from MIRT [3] for comparison. Fig.3.15-Fig.3.17, report the results of different registration using affine, demons and cubic-BSpline transformation using SSD on three subjects. The algorithms using Affine + Demons consistently out performs the other transformation models.

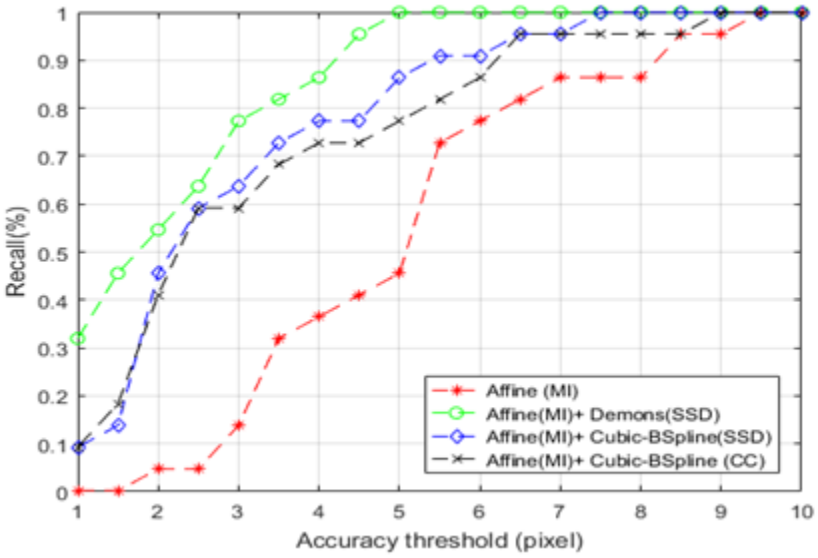

Figure 3.15: Qualitative comparison of image registration using affine, Demons and cubic BSpline model (Face Region)

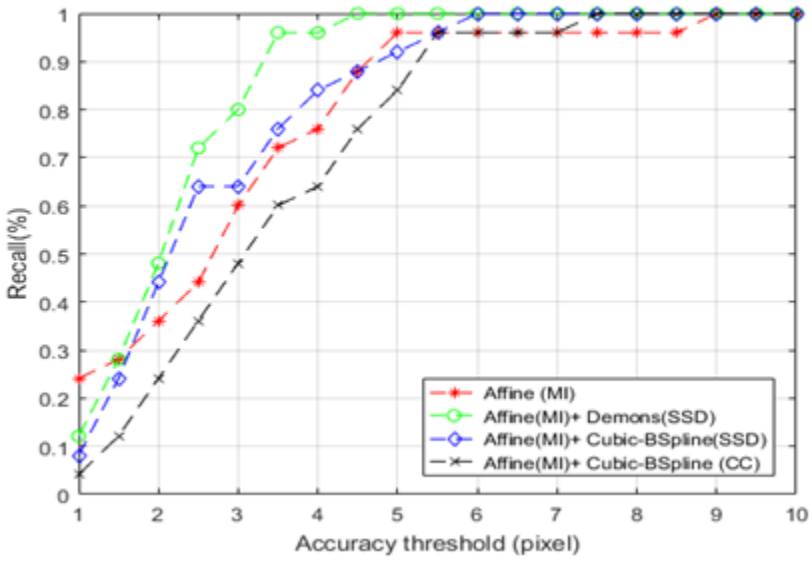

Figure 3.16: Qualitative comparison of image registration using affine, Demons and cubic BSpline model (Face Region)

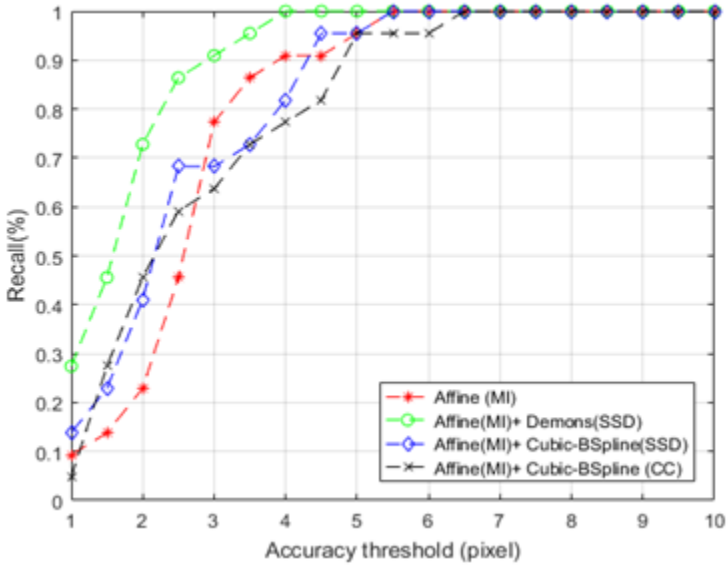

Figure 3.17: Qualitative comparison of image registration using affine, Demons and cubic BSpline model (Face Region)

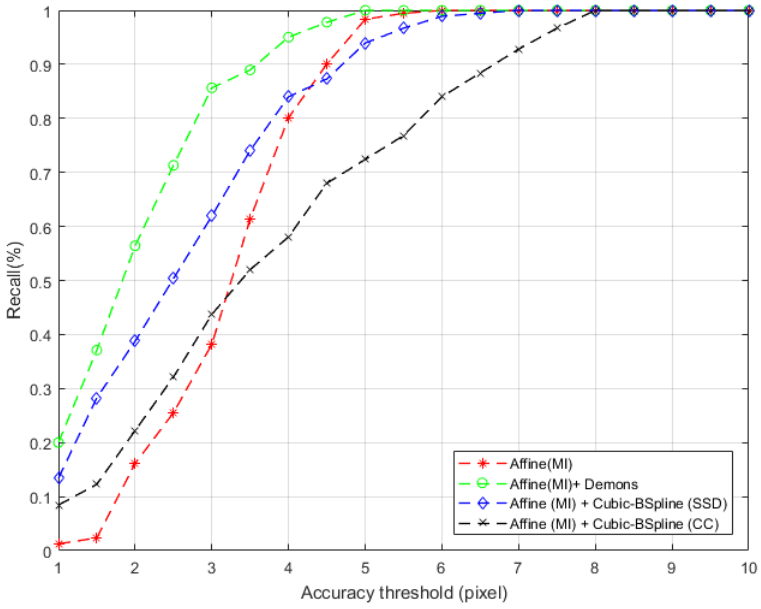

Figure 3.18: Qualitative comparison of image registration using affine, Demons and cubic BSpline model (Eye Region)

Table 3.2: Registration Matching Error-Eye Region (in pixels)

Methods/Algorithm (Similarity Metric)	Sub. No. 1	Sub. No. 2	Sub. No. 3
Affine (MI)	2.84	3.46	2.89
Affine (MI) + Demons (SSD)	1.75	2.44	2.22
Affine (MI) + Cubic B-spline (SSD)	3.86	2.84	2.93
Affine (MI) + Cubic B-spline (SSD)	4.34	2.83	2.50

3.3.2 Canthi Temperature Measurement

A recent study [30] on IR thermal imaging for mass blind fever screening and IEC 80601-2-59:2008 indicates inner canthi as the most stable temperature with good co-relation for measuring body temperature. In this study, we compare the automated registration-based approach for inner canthi temperature measurement with manual measurement. This comparison validates the registration-based approach as a viable means of temperature measurement using inner canthi. We use the DRMF-based model [4] for fiducial point detection as a tool for canthi detection. These results can be used to study the correlation between canthi temperature and febrile patients and decide on optimal temperature threshold. This is still an active are of research and we will focus on automation of canthi temperature measurement. We study temperature in three regions (i) Left Canthi (ii) Right Canthi and (iii) Fore Head regions as shown in Fig.3.21.

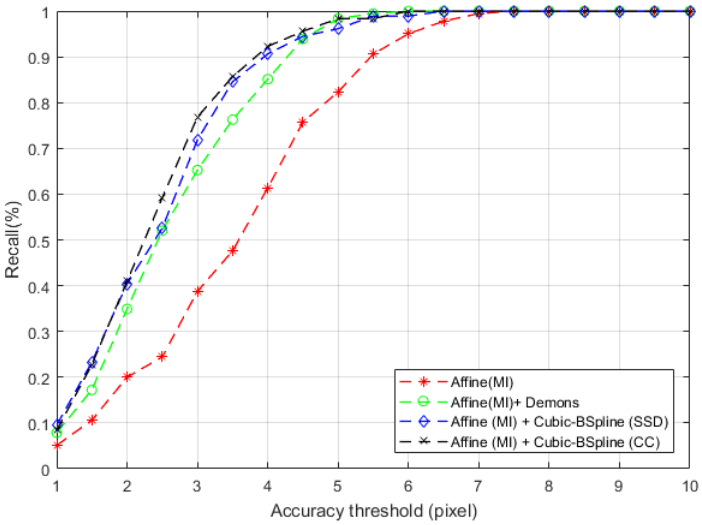

Figure 3.19: Qualitative comparison of image registration using affine, Demons and cubic BSpline model (Eye Region)

We use Bland Altman plots [36] for combined graphical and statistical interpretation of the two measurement techniques. We plot correlation and Bland Altman plots to highlight the difference between the measurements against their mean as shown in Fig.3.24 and Fig.3.25. The mean and standard deviation (SD) of the differences, mean of absolute differences and the 95 (percent) limits of normal distribution ($\pm$ 1.96SD) are calculated. The root mean square error (RMSE), Pearsons correlation coefficients and the corresponding p-values were calculated for estimation of inner canthi temperature from manual and registration based methods.

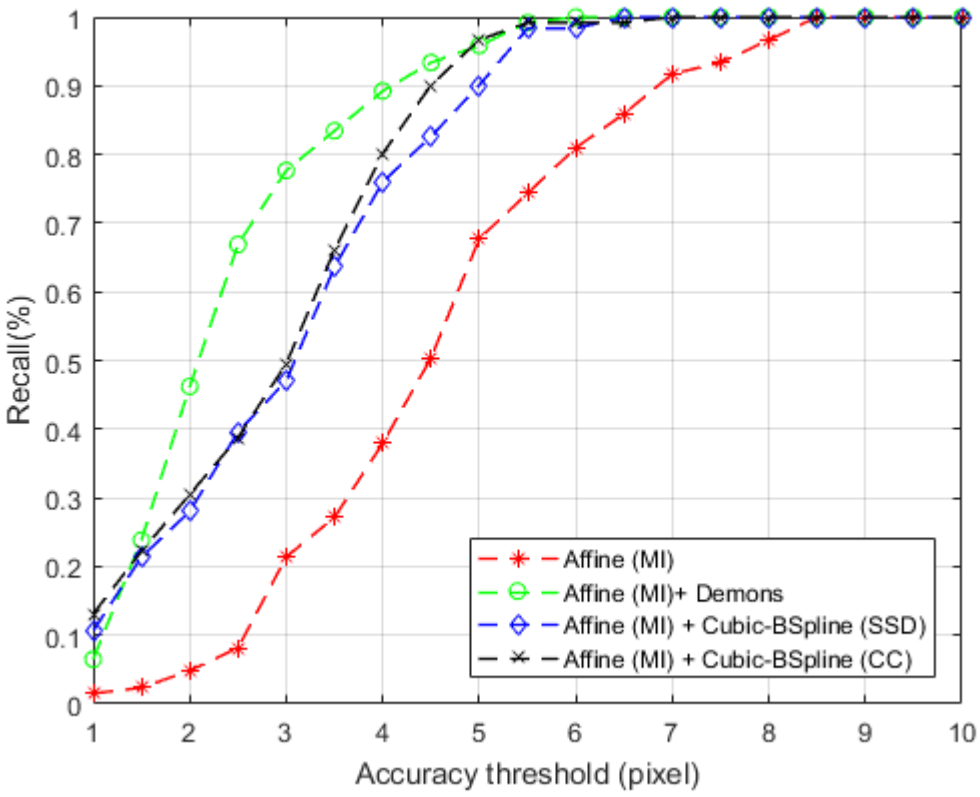

Figure 3.20: Qualitative comparison of image registration using affine, Demons and cubic BSpline model (Eye Region)

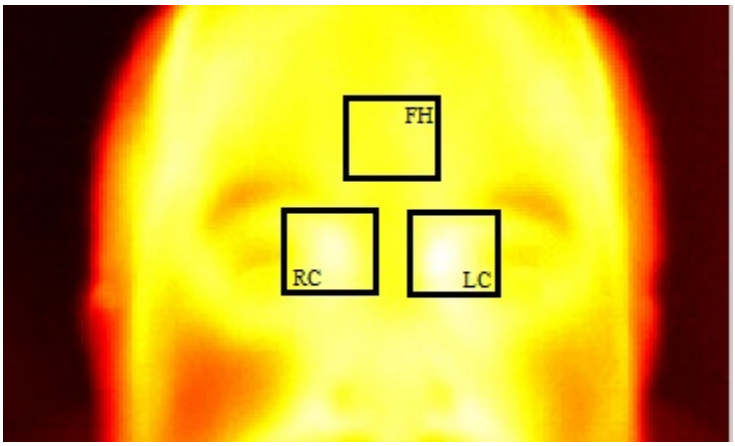

Figure 3.21: Temperature measurement (a) Fore Head (FH) (b) Left Canthi (LC) and (c) Right Canthi (RC)

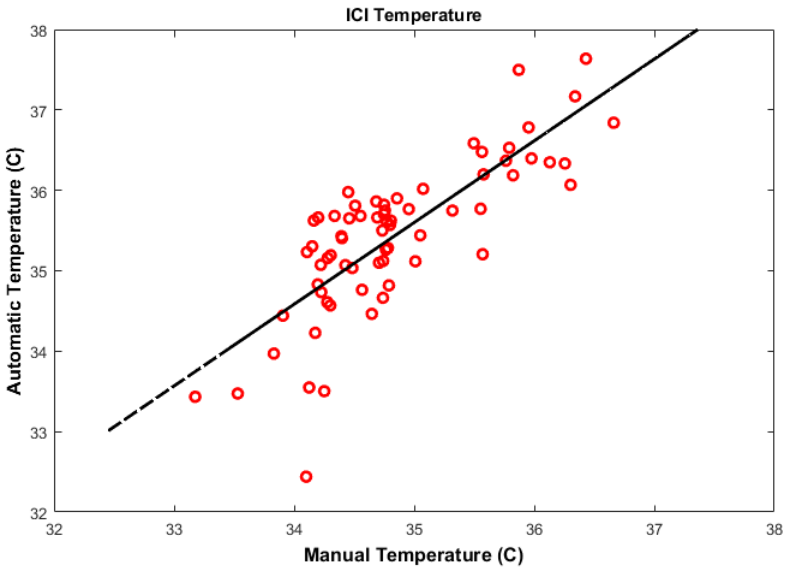

Figure 3.22: ICI Temperature measurement (a) Fore Head (FH) (b) Left Canthi (LC) and (c) Right Canthi (RC)

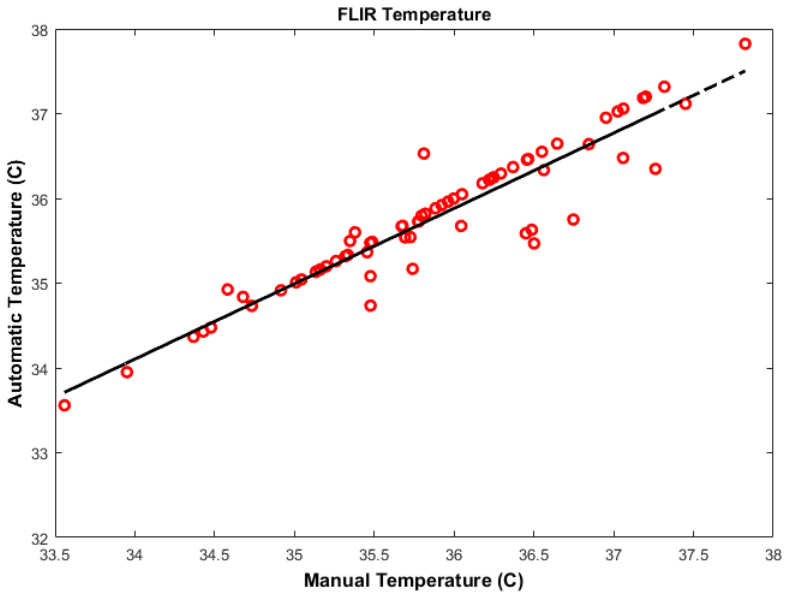

Figure 3.23: FLIR Temperature measurement (a) Fore Head (FH) (b) Left Canthi (LC) and (c) Right Canthi (RC)

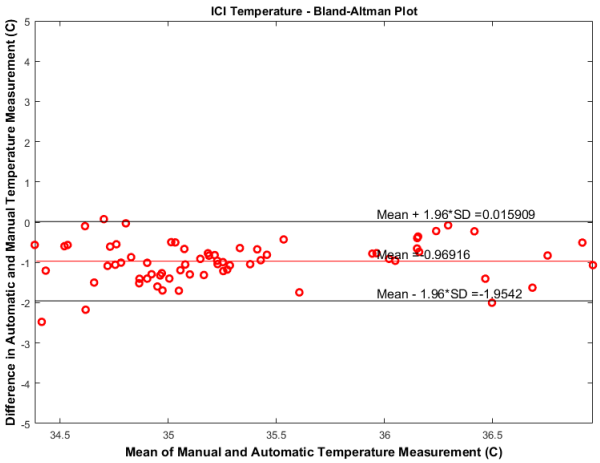

Figure 3.24: Bland Altman - ICI Temperature measurement (a) Fore Head (FH) (b) Left Canthi (LC) and (c) Right Canthi (RC)

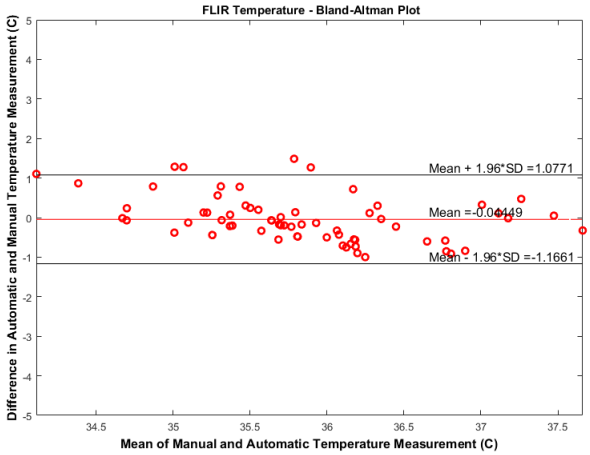

Figure 3.25: Bland Altman - FLIR Temperature measurement (a) Fore Head (FH) (b) Left Canthi (LC) and (c) Right Canthi (RC)

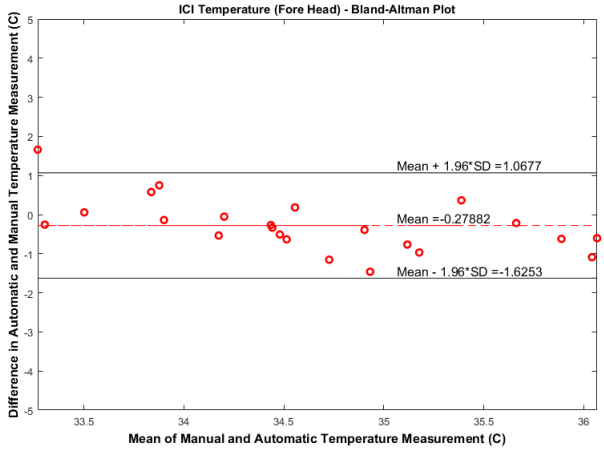

Figure 3.26: Bland Altman - ICI Temperature measurement in Fore Head (FH)

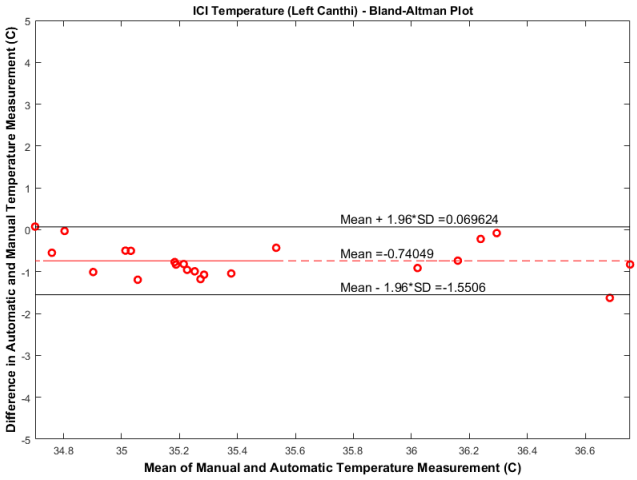

Figure 3.27: Bland Altman - ICI Temperature measurement in Left Canthi (LC)

Table 3.3: ICI Temperature Measurement using Inner Canthi

ICI Temperature (C) Subject No.	LC	RC	FH
1	35.6524	35.1175	33.4333
2	35.0344	35.0698	33.9702
3	35.7484	36.0187	35.0992
4	35.8611	35.4407	34.4643
5	35.9	35.7665	34.8306
6	35.4065	35.1227	34.4418

Table 3.4: FLIR Temperature Measurement using Canthi

FLIR Temperature (C) Subject No.	LC	RC	FH
1	35.3651	34.9885	33.7018
2	34.7355	34.7389	34.0689
3	35.4691	35.2094	34.4660
4	35.5427	35.2094	34.4660
5	35.5873	35.5339	34.9206
6	35.1689	35.0156	34.6022

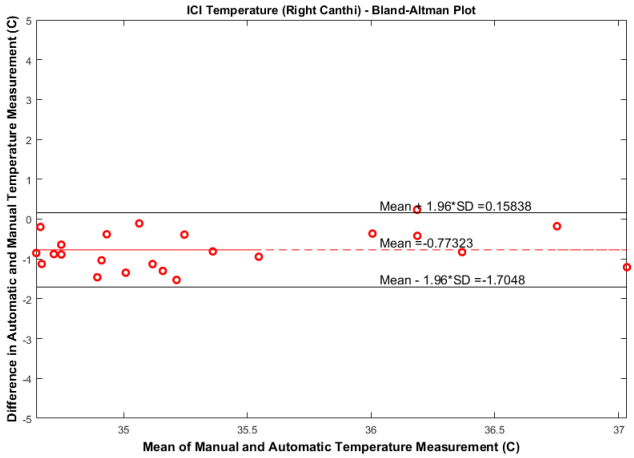

Figure 3.28: Bland Altman - ICI Temperature measurement in Right Canthi (RC)

Table 3.5: Statistics of Temperature Measurement (Automatic vs Manual)

Thermal Camera (C)	LC (Mean ± 1.96SD)	RC (Mean ± 1.96SD)	FH (Mean ± 1.96SD)
ICI	-0.740 ± 0.80	-0.773 ± 0.93	-0.278 ± 1.34
FLIR	0.304 ± 0.90	0.387 ± 1.04	0.701 ± 0.77

Chapter 4: Imaging Photoplethysmography (IPPG)

4.1 Overview

Non-contact IPPG has made advancement in the last few years towards monitoring vital signals through consumer grade video recording. This represents a significant advancement in clinical methods for monitoring vital signals. Traditional methods include contact based methods preventing long term patient monitoring. Non-contact IPPG is widely researched due to its feasibility and low cost applications. The earliest research on IPPG was reported in 2005, which discusses extraction of PPG signal from subjects wrist [47]. These were the first experiments towards obtaining PPG signals from a video camera. Similar experiments were conducted with LED illumination and CMOS cameras directed at subjects inner arm [15]. Later in 2008, a paper demonstrated the extraction of PPG signals through video recording in ambient light with commercial grade cameras using fast Fourier transform (FFT). This is used to extract the heart rate frequency from mixed frequency content of video, giving scope to potential usage in clinical setting [45]. Poh *et al.* [39] published papers that examined using a standard webcam built into their laptop, to extract PPG signal from subjects of different skin colors [39]. Many such studies studied estimation of PPG signal with digital cameras, mobile phones [42] and webcams [5].

This is a clear trend in the potential application and many efforts are being made to use these methods in clinical setup. Non-contact reflectance mode IPPG uses ambient light and are showing promising insights into future of non-contact fever screening and many other applications [45]. It provides non-invasive/remote measurement of cardiac pulse, without the use of any electrodes. In non-contact PPG signal is extract from conventional consumer grade video recording equipment. The physiological parameters, like heart and respiratory rates, can be extracted using video recording equipment to film the brightness variations in someones skin. The underlying principle for the observed signal is a complex function of blood volume, volumetric change in blood vessels and other physiological parameters, which is an active area of research. However, the short duration of video sequence and linear model assumption has shown to give reasonable results [45] for heart rate estimation. Hence, a performance evaluation of feasibility and accuracy of these methods across different parameters is an interesting study, which enables wide range of applications. All these methods involve video recordings for different subjects under ambient light with a duration of 30 seconds to few minutes. In case of IPPG recordings using a RGB color space, green channel shows clear heart rate pulsations where the absorption is highest [49]. The average of Red, Green and Blue channels within ROI across frames gives a raw signal, which shows modulation with heart rate. The modulation of reflected ambient light depends on the pigments in the skin, bone, and blood flow through veins. A clear trend in the absorption when blood volume changes in arteries and arterioles. This shows a PPG signal as AC signal modulated over a DC component. These reflection intensities are highly sensitive motion

artifacts and show poor signal-to-noise ratio (SNR). Moreover, different image processing algorithms used in the video acquisition system have significant influence on the performance of heart rate estimation. This work studies the performs of IPPG for different frame rates and different ROI.

4.2 Implementation/Methods

4.2.1 Experimental Setup

In the setup for video recording the subject was asked to sit on a chair in front of camera to minimize any movement artifacts. The recorded video from two image capture tools for this study, built-in camera in iPhone 7 (Apple inc, USA) and DSLR Cannon iT3 digital camera. The camera was mounted on tri-pod and recorded the regions around face of the subject with typical ambient day light as source of illumination along with fluorescent light. These videos were recorded with 24-bit RGB (3 channels and 8 bits each) at 60 frames per second (fps) with a resolution of 1280x720. The videos were saved in .mov format. These videos were taken with the subjects within 1 meter of skin surface. The experiments were conducted indoors and outdoor with adequate sunlight as the only source of illumination. The subjects were seated to minimize movement at a distance of 0.5 meters from the mobile camera used for recording. During the shoot the subjects were asked to minimize movement and look directly into the recording camera. A contact based measurement was used for validation of measurement using image photo plethysmography (IPPG).

4.2.2 Signal Extraction

The recorded video was loaded into MATLAB (The MathWorks, Inc.) workspace, and manual selection of ROI was done to localize the measurement region within the face video. The red (R), green (G) and blue (B) channels of the ROI region were separated and spatially averaged to yield time series signals R(t), G(t) and B(t) respectively. Average values of pixels within ROI is used to improve the SNR and apply Fourier analysis to estimate the frequency spectrum contents of the time-varying signal. The normalized raw RGB signals are as follows:

$$G'(t) = (\frac{G(t) - \mu_G}{\sigma_G}) \tag{4.1}$$

Similarly normalized curves for red ($R(t)$) and blue ($B(t)$) channels, where μ and σ are the mean and standard deviation of respective channels. These normalized traces had zero-mean and unit variance as shown in Fig.4.1.

For pulse amplitude mapping each frame of the image was divided into coarse grid of square boxes with a user defined block size. Spatial averaging in such coarse grid improves the SNR of the signal. It displays the power spectrum values of each block at heart rate frequency to visualize the 'power map' and try to analyze the effects of different block size.

4.2.3 Heart Rate Estimation Algorithm

The time series signal is divided into 30s moving window with 29s overlap. The spectrum analysis of all the windows is used for the estimation of heart rate.

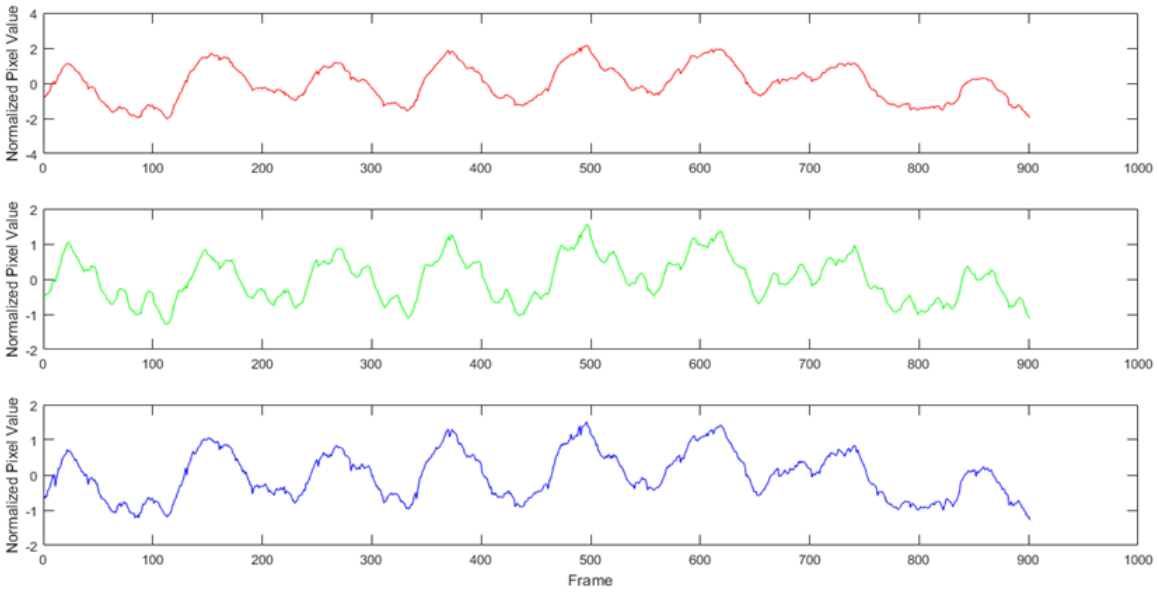

Figure 4.1: Red, Green and Blue Channel indicating Normalized pixel values used to estimate heart rate

The spectrum of the extracted green channel shows clear pike at the heart rate frequency. As shown in Fig.4.2, one of the highest peaks also corresponds to likely frequency range for cardiac cycle, where 1.2 Hz = 72 beats per minute (bpm). Heart rate (HR) is defined as the number of beats per minute (bpm) and is normally in the range of 40 to 240 bpm. HR is usually divided into two modes of operation, (i) first when the body is at rest without a physical strain the heart rate is in the range of 60-100 bpm and (ii) other operating range is when the body is under pressure with the heart rate in range of 60 bpm to maximum possible HR, which is dependent on age, sex and physical fitness, which generally lies in the range of 180 +/- 20 bmp.

The videos were recorded with subjects under good lighting condition and resting position to avoid any external artifacts. This simplifies the pre-processing

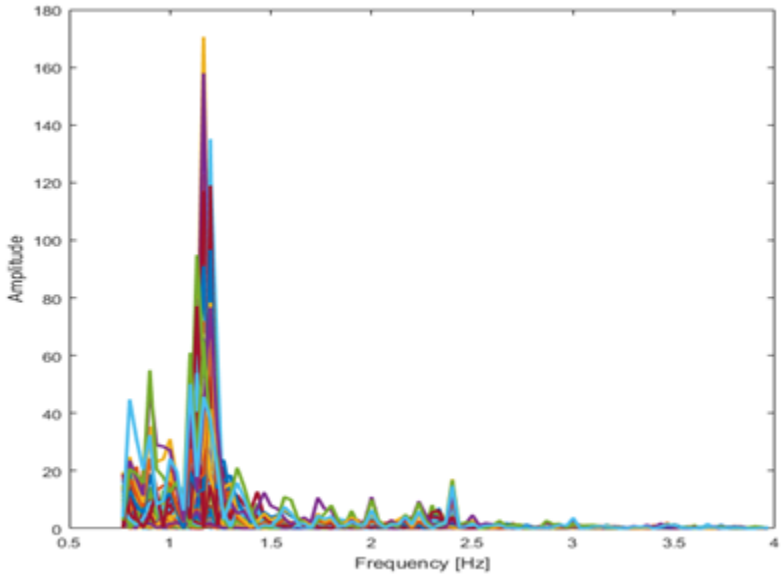

Figure 4.2: Heart rate frequency Spectrum within (0.75,4) Hz frequency range

needed for the video sequence. The ROI was selected manually and the average values of Red, Green and Blue channels across frames. Observed modulation with heart rate in the green channel significantly compared to the red or blue channel, as explained by the absorption spectrum of haemoglobin. The spatial averaging approach was effective and showed promising results. The heart rate was estimated from spectrum of time-varying signal as shown Fig.4.3. The HR was obtained as the most frequently occurring HR (mode) of the HR measurement from different windows.

These methods are found to adequate, robust and efficient for processing of recorded visible video. Research [36], suggests the use of Independent Component Analysis (ICA) in extracting photoplethysmography(PPG) heart rate information

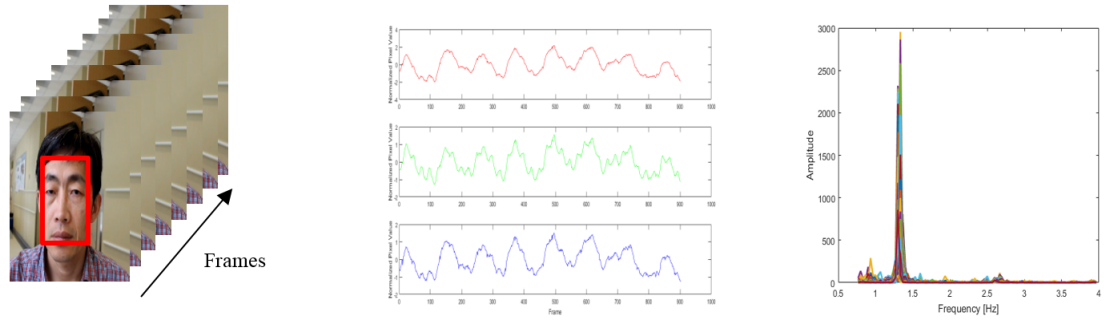

Figure 4.3: Heart rate frequency Spectrum within (0.75,4) Hz frequency range

and back this with experimental results. ICA, in this study is applied to signal extracted from a video segment using detection videos. The further study, influence of applying ICA-JADE [8, 41] for different ROI with varying frame rates and window size. This enables to estimate potential requirements for reliable heart-rate measurement specifically the impact of video parameters and their influence on heart rate estimation.

4.2.3.1 Independent Component Analysis

The PPG signal of interest is the cardiovascular pulse wave that propagates through body. The changes in blood flow and volumetric changes in blood vessels during such cardiac cycles modify the path of incident ambient light. The recorded video contains a mixture of underlying PPG signal along with other sources of fluctuation that include artifacts due to motion or change in ambient lighting conditions. These observed signals record a mixture of original PPG signal with different con-

tributions to red, green and blue color sensors. Conventional ICA is a special case of wider concept of blind source separation (BSS), which assumes a linear transformation of original source signals. ICA assumes that number of recoverable signals cannot exceed the number of observations and can be expressed as :

$$x(t) = Ms(t) \tag{4.2}$$

where the vectors $x(t) = [\ R(t)\ G(t)\ B(t)\ ]^T$, $s(t) = [\ s_1(t)\ s_2(t)\ s_3(t)\ ]$ and the square 3x3 matrix M contains mixture coefficients. The ICA tries to find the W matrix that separates the signal, it is equivalent to inverse of mixing matrix M, given $x(t)$.

$$s(t) = Wx(t) \tag{4.3}$$

$$[s(1),\ s(2),\ s(3)] = M^{-1}.[x(1),\ x(2),\ x(3)] \tag{4.4}$$

where $x(t)$ is the vector of observed signals and $s(t)$ is an estimate of the underlying physical signals. W is found in ICA as the matrix maximizing some measure of statistical independence of the components in $s(t)$. The underlying principle based on central limit theorem, which suggests a sum of independent random variables is more gaussian than the original variable. Thus W tries to maximize the non-gaussianity of each source signal. The most widely used measures include non gaussianity of the variables, a property that (by central limit theorem) implies independence. This can be achieved through iterative solutions that try to maximize

or minimize cost functions that measure approximations of non-gaussianity through kurtosis [41], negentropy [41] or mutual information [41].

As mentioned above, different iterative algorithms can be used for ICA depending on the criteria for statistical independence. FastICA [16], InfoMax [6] and Joint Approximation Diagonalization of Eigenmatrices (JADE) [41] are among the few widely used algorithms for ICA. Depending on the data to be analyzed, different algorithms are preferred publications [25, 27, 28] give a comparison of different ICA algorithms. All these methods try to approximate the demixing matrix (W) which is the approximation of the inverse of mixing matrix (M). JADE algorithm implementation in MATLAB [41], based on its computational advantage of using matrix computation involving matrix diagonalization similar to Principle Component Analysis [**?**]. JADE is most widely used for ICA and shows consistent and reliable results. It uses fourth-order "cumulants" array from the data and the details of the algorithms can be reviewed in [41]. It works by giving the original signals as MATLAB row vectors. It then analyzes the recordings and outputs the so called W matrix, which is used to extract original sources from observations. To summarize the Heart rate estimation algorithm is as follows:

4.2.4 Pulse Amplitude Mapping

The video recording was loaded into the MATLAB workspace. The MATLAB maps the relative pulse amplitudes in the Green channel by diving the frames into grids of required block size. The algorithms for pulse amplitude mapping is as fol-

Algorithm 2 Heart Rate Estimation

1: Construct video object with resolution 1280x720 pixels, color space 24-bit RGB and frame rate 60 fps
2: Capture single frame and perform ROI selection using user selected rectangle
3: Record N seconds of this ROI and average contents of green channel for each frame
4: (Optional) Apply ICA to estimate the source signals for R, G and B channels
5: Calculate PSD and detect its peak in the interval [0.75 4] Hz i.e. [40 240] bpm
6: Track the heart rate measurement within 10% variation of previous reading as valid measurement
7: Calculate the mode of heart rate estimated from different windows

lows:

Pulse amplitude maps (Power maps) within region of interest are useful tools to estimate regions with strong heart rate signal and identify motion artifacts [45]. The skin regions around forehead and cheeks show clear contrast in power maps for heart rate estimation compared to the surroundings.

4.3 Results and Analysis

The video processing and analysis of measurement was done in MATLAB. An overview of the heart rate estimation is shown in Fig.4.7. In case of face video recording selected the face region as ROI manually, then the video was processed as three separate channels red, green and blue. The pixels value within the ROI

Algorithm 3 Pulse Amplitude Mapping

1: Construct grid dividing the video frame into non-overlapping square regions. The size of these blocks(blockSize) is a trade off between signal to noise ratio and resolution

2: Average the pixel values in each box across frames to generate the time series signal, which are later normalized to zero mean and unit standard deviation

3: Record N seconds of this ROI and average contents of green channel for each frame

4: (Optional) Apply ICA to estimate the source signals for R, G and B channels

5: For each block calculate the FFT using the normalized/estimated (G/G') green channel (after ICA).

6: Calculate Power Spectrum Density (PSD) and detect its peak in the interval [0.75 4] Hz (i.e. [45 240] bpm),

7: Track the heart rate measurement within 10% variation of previous reading as valid measurement, heart rate is the mode of peaks detected in different boxes

8: Select the power spectrum values at the heart rate estimated from different grids in ROI and updated the grid values to generate the power map as shown Fig.**??**

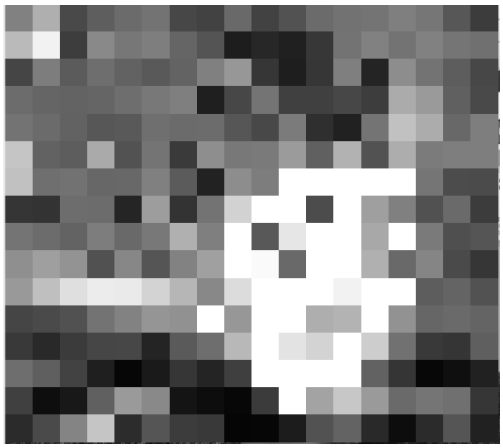

Figure 4.4: Pulse Amplitude Map at Heart rate frequency with 50x50 grid size

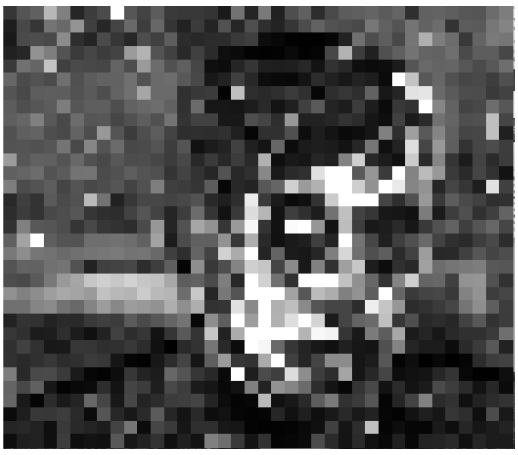

Figure 4.5: Pulse Amplitude Map at Heart rate frequency with 25x25 grid size

Figure 4.6: Pulse Amplitude Map at Heart rate frequency with 10x10 grid size

were averaged to give reading of the red, green and blue channels across frames. These red, green and blue traces are normalized to extract the AC signal over the DC. These normalized signals are used for FFT analysis. FFT Spectrum analysis was done using normalized signals using normalized signals over a window width of 30 seconds and 29 seconds overlap, followed by peak detection for Pulse frequency estimation. To remove outliers due to motion artifacts any change in heart rate of more than 10% in either direction from one window to another was considered an error and alternative peaks were used to detect heart rate. Peak detection was done within windows of 0.75 Hz to 4 Hz corresponding to 45 to 240 bpm.

An example of estimating heart rate from video recording is shown in Fig.4.7. The estimation of heart rate of a subject at rest with video recording for 2 minutes duration. It also shows the 30s window of RGB traces after normalization. Fig.4.7 shows the 30s windows of the RGB traces obtained by averaging pixel values in ROI. Observe PPG signal as an AC modulation over the DC signal. The power spectrum

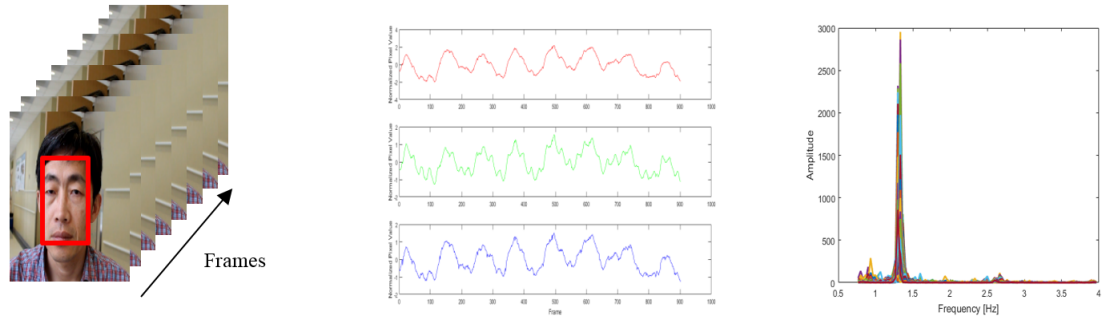

Figure 4.7: Heart rate estimation (a) ROI Selection (b) Time Series signal and (c) Frequency Spectrum

of the green channel after ICA-JADE shows a clear peak at 1.13 Hz indicating heart rate along with some harmonics. A clear peak in the power spectrum indicating heart rate. To evaluate the effect of ICA on estimating heart rate directly from the green channel and after applying ICA-JACE algorithm for heart rate estimation.

We use Bland-Altman analysis 4.7, the mean error varired from ± 1.18 bpm to ± 9.07 bpm. The limits of agreement (95%) ± 1.96SD was ± 1.63 bpm to ± 11.67 bpm. The root mean square error(RMSE) was observed to vary from 2 bpm to 14.73 bpm. The comparative study was done on three different ROI with different frame rates. We evaluate the improvement in estimation with raw green channel, window size and frame rate.

4.3.1 Heart Rate Measurement from Face Region

In the video loaded into MATLAB, selection of face regions was done manually as shown in Fig.4.8. The face regions used for selection is 60% width and height of the

Table 4.1: Effects of ROI on Heart Rate Estimation without ICA

Heart rate (bpm) Subject No.	contact PG	Face	Fore Head (FH)	Cheeks
1	79.68	78 ± 2.26	78 ± 2.36	78 ± 2.23
2	79.35	78 ± 1.61	78 ± 2.24	78 ± 1.60
3	84.19	80 ± 12.13	80 ± 14.17	80 ± 11.78
4	86.83	82 ± 8.61	50 ± 15.30	82 ± 11.74
5	78.34	76 ± 12.95	76 ± 6.62	48 ± 10.12
6	65.45	62 ± 6.49	62 ± 6.72	60 ± 6.30
7	65.40	64 ± 7.25	64 ± 7.13	64 ± 5.52

face [37]. The PPG signal was extracted from the face region on each frame. The face is selected since it contains most of the microvascular bed of tissues that are exposed to the environment. The microvascular bed of tissue is the main source of IPPG. As shown in Fig.2, when the light (i.e. comprise of red, green, blue color spectrum) falls on the skin tissue, many substance such as pigments in the skin, bone, and arterial and venous blood absorbs the light. The main absorption occurs due to blood volume changes in the arteries and arterioles (but not in the veins). Therefore, the reflected signal from the skin adopts a photoplethysmographic waveform, consisting of direct current (DC) and alternating current (AC) components.

Table 4.2: Effects of ROI on Heart Rate Estimation with ICA

Heart rate (bpm) Subject No.	contact PG	Face	Fore Head (FH)	Cheeks
1	79.68	78 ± 4.95	78 ± 6.07	78 ± 2.29
2	79.35	78 ± 3.41	80 ± 8.97	78 ± 4.85
3	84.19	80 ± 14.23	80 ± 15.10	80 ± 13.90
4	86.83	82 ± 15.85	50 ± 12.65	82 ± 17.15
5	78.34	50 ± 12.03	48 ± 11.60	48 ± 9.28
6	65.45	50 ± 12.03	48 ± 11.60	48 ± 9.28
7	65.40	48 ± 6.11	48 ± 6.72	50 ± 6.84

4.3.2 Heart Rate Measurement from Fore Head Region

The Fore head regions selections is based on [33] as shown in Fig.4.9, which usese the upper portion of the face just above eyes.

4.3.3 Heart Rate Measurement from Cheek Region

The third ROI is face regions below eyes, which highlights the low part of the face regions as shown in Fig.4.6, have strong heart rate signal.

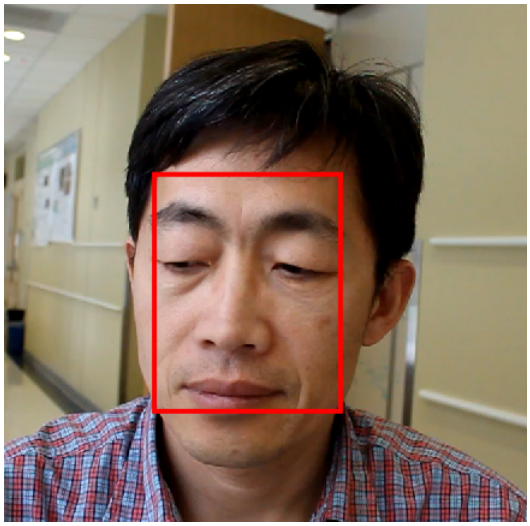

Figure 4.8: ROI Selection for IPPG - Face Region

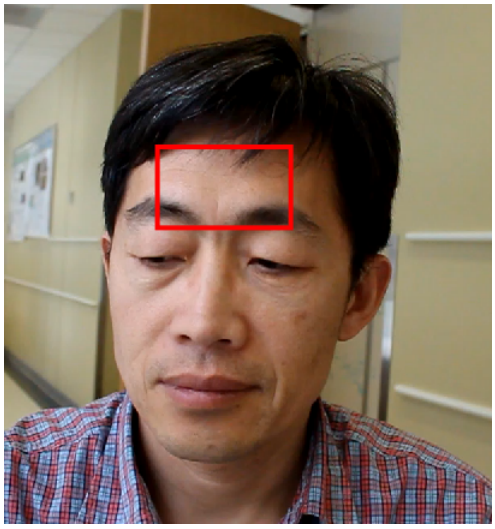

Figure 4.9: ROI Selection - Fore Head Region

Table 4.3: Performance measure of IPPG on Face Region

Heart Rate Estimation (bpm) Subject No.	cPPG	IPPG	Mean Error	SD Error	RMSE
1	79.68	78	-2.65	2.25	3.47
2	78.34	76	-9.07	11.67	14.73
3	65.45	62	-8.35	6.51	10.56
4	79.35	78	-1.18	1.633	2.00

Table 4.4: Effects of Frame rate on Heart Rate Estimation (Face Region)

Heart rate Subject No.	contact-PG	60 fps	30 fps	15 fps	10 fps
1	79.68	78 ± 2.12	76 ± 2.08	78 ± 2.10	78 ± 3.10
2	79.35	78 ± 1.61	76 ± 1.82	80 ± 3.63	80 ± 3.65
3	84.19	80 ± 12.08	78 ± 11.13	80 ± 14.55	54 ± 12.24
4	86.82	82 ± 15.73	82 ± 14.69	84 ± 15.76	50 ± 8.69

Table 4.5: Effects of Window Size on Heart Rate Estimation (Face Region)

Heart rate Subject No.	contact-PG	30 sec	15 sec	10 sec
1	79.68	78 ± 2.12	78 ± 2.12	78 ± 4.64
2	79.35	78 ± 1.61	78 ± 2.10	78 ± 4.33
3	84.19	80 ± 11.9	81 ± 8.88	78 ± 13.13
4	86.82	82 ± 15.56	84 ± 14.84	84 ± 14.59

Table 4.6: Performance measure of IPPG on Fore Head Region

Heart Rate Estimation (bpm) Subject No.	cPPG	IPPG	Mean Error	SD Error	RMSE
1	79.68	78	-2.79	2.46	3.71
2	78.34	76	-4.55	6.3002	7.74
3	65.45	62	-10.48	5.41	11.78
4	79.35	78	-2.53	6.31	6.77

Table 4.7: Effects of Frame rate on Heart Rate Estimation (Fore Head Region)

Heart rate Subject No.	contact-PG	60 fps	30 fps	15 fps	10 fps
1	79.68	78 ± 2.17	76 ± 2.03	78 ± 2.21	78 ± 5.11
2	79.35	78 ± 2.24	76 ± 4.20	80 ± 7.99	78 ± 14.34
3	84.19	80 ± 14.09	78 ± 13.68	82 ± 15.61	54 ± 12.24
4	86.82	48 ± 13.82	46 ± 15.87	48 ± 8.16	50 ± 4.20

Table 4.8: Effects of Window Size on Heart Rate Estimation (Fore Head Region)

Heart rate Subject No.	contact-PG	30 sec	15 sec	10 sec
1	79.68	78 ± 2.23	78 ± 3.32	78 ± 6.24
2	79.35	78 ± 2.24	78 ± 5.32	78 ± 8.12
3	84.19	80 ± 14.09	81 ± 13.35	78 ± 12.1
4	86.82	48 ± 13.82	57 ± 15.67	48 ± 14.12

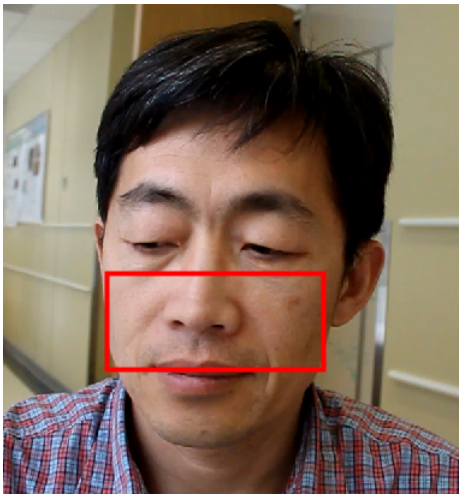

Figure 4.10: ROI Selection - Cheek Region (Lower Face)

Table 4.9: Performance measure of IPPG on Cheek Region

Heart Rate Estimation (bpm) Subject No.	cPPG	IPPG	Mean Error	SD Error	RMSE
1	79.68	78	-2.73	2.25	3.53
2	78.34	76	-13.07	13.01	18.39
3	65.45	62	-21.22	8.12	22.70
4	79.35	78	-1.16	1.61	1.98

Table 4.10: Effects of Frame rate on Heart Rate Estimation (Cheek Region)

Heart rate Subject No.	contact-PG	60 fps	30 fps	15 fps	10 fps
1	79.68	78 ± 2.08	76 ± 2.02	78 ± 2.10	78 ± 3.53
2	79.35	78 ± 1.59	76 ± 1.82	80 ± 1.92	80 ± 3.45
3	84.19	80 ± 11.72	78 ± 12.07	48 ± 15.63	48 ± 12.49
4	86.82	82 ± 10.10	84 ± 9.18	84 ± 17.23	84 ± 16.74

Table 4.11: Effects of Window Size on Heart Rate Estimation (Cheek Region)

Heart rate Subject No.	contact-PG	30 sec	15 sec	10 sec
1	79.68	78 ± 2.07	78 ± 3.29	78 ± 4.45
2	79.35	78 ± 1.60	78 ± 2.12	78 ± 4.57
3	84.19	80 ± 11.47	81 ± 11.03	78 ± 11.77
4	86.82	82 ± 10.10	84 ± 11.34	84 ± 12.97

Chapter 5: Conclusion

5.1 IR Thermography

In this thesis, we focused on MMIR of IR and visible face images for fever screening. Especially for accurate alignment of non-planar surfaces like face image, we used free form deformation (FFD) models to improve registration accuracy after affine transformation. We exploited the idea of matching IR and visible images using edge maps, which gives us an effective criterion for estimating FFD transformation. The quantitative measure of accuracy, obtained through selected control point correspondence, is within $\pm$ 2.3 mm which enables accurate localization of canthi region. The qualitative comparison on images show comparison of affine transformation with FFD based on Demons algorithm and Cubic B-spline registration, which are quite widely used in medical imaging. Based on the results, Demons algorithm outperforms Cubic B-spline registration, which can be attributed to over-fitting on the outliers, which degrades the matching accuracy of B-spline registration in canthi region.

In this study we try to compare the automated registration based approach for inner canthi temperature measurement with manual measurement. This comparison validates the registration based approach as a viable means of temperature

measurement using inner canthi. We use DRMF [4] based model used for fiducial point detection as a tool for canthi detection. We study temperature in three regions (i) Left Canthi (ii) Right Canthi and (iii) Fore Head regions. We use Bland Altman plots [36] for combined graphical and statistical interpretation of the two measurement techniques. These plots are used to plot the difference between the measurements against their mean. The mean error of - 0.773 (C) temperature and $\pm$ 1.04 (C) temperature of 95% limits of normal distribution (+/- 1.96SD) are calculated. These results show promising results for automatic canthi based temperature measurement for blind mass fever screening.

5.2 Image Plethysmography

In this thesis, we study the heart rate extraction using mobile camera video of the subject using just ambient light. We try to validate the measurement method using pulse amplitude mapping. We investigate the performance of the heart rate estimation based on different video parameters like frame rate, resolution, time windows and different grid sizes for pulse amplitude mapping. A clear signal was extracted from manual segmentation of ROI. These methods can be automated through simple face detection/tracking algorithms. The spectrum of video signal shows several harmonics to base HR frequency. The ICA algorithm as studied in [45], shows improvement in heart rate estimation especially for noisy signals by removing lower-frequency disturbances. The observed performance of heart rate estimation shows a mean error of 2.01 bpm and 5.31 bpm of 95 % limits for error measurement

(mean ± 1.96 SD), compared to contact based PPG. Pulsativity mapping, from a video with minimum movement shows the cleanest signal. The pulsativity (pulse amplitude mapping) shows good validation for the estimated heart rate by showing strong signal in the face regions compared to surroundings especially for the forehead and cheeks. It is useful for mapping regions with strong PPG signal or discarding regions with less pulsatile signal.

Moreover, several parameters were seen to have influence on the quality of the acquired pulsating signal. The quality of the PPG signal observed from video is severely restricted by illumination changes, movement artifacts and noise. These studies clearly show the possibility of estimating heart rate from commercial grade video recording. The experiments with frame rate varying from 60 fps to 10 fps, show good consistency, enabling accurate estimation of heart rate from low grade video recording. After analysis with different ROI selection, the fore head regions is found to be stable site for estimation of heart rate. Hence, the results show good promise in implementation of IPPG for heart rate monitoring especially for mass fever screening as a possibility, where low cost of installation and flexibility are important.

Appendix A: Results Analysis

A.1 Bland-Altman Analysis

The Bland-Altman analysis/plot is used as graphical method to compare two measurement techniques. This includes plots between difference of two measurements agianst the mean of the two measurements. These plots are used to identify the mean difference and 95% limits under the assumption of gaussian distribution i.e. mean $\pm$ 1.96 SD of the difference. These plots can be used to measure any systematic bias between the magnitude of the measurement and error. The underlying observation in such plots is the mean $\pm$ 1.96 SD, if the values of these limits is clinically acceptable the two methods can be used interchangeably.

A.2 Recall Graphs

We evaluate recall graphs to have quantitative evaluation of registration accuracy. We measure the Euclidean distance between the landmark in the transformed moving points and corresponding landmarks in reference image. We compute recall on all the landmark pairs of regions as metric used in [21]. The true positive rate, is defined as the fraction of true positive correspondences, which is defined as when

two corresponding pairs fall within a given accuracy threshold in terms of pairwise distance.

Bibliography

[1] IEC 80601-2-59 : MEDICAL ELECTRICAL EQUIPMENT - PART 2-59: PARTICULAR REQUIREMENTS FOR THE BASIC SAFETY AND ESSENTIAL PERFORMANCE OF SCREENING THERMOGRAPHS FOR HUMAN FEBRILE TEMPERATURE SCREENING.

[2] WHO — Assessment of risk associated with influenza A(H5N8) virus. *WHO*, 2017.

[3] Andriy Myronenko. Medical Image Registration Toolbox - Andriy Myronenko.

[4] Akshay Asthana, Stefanos Zafeiriou, Shiyang Cheng, and Maja Pantic. Robust Discriminative Response Map Fitting with Constrained Local Models.

[5] Frédéric Bousefsaf, Choubeila Maaoui, and Alain Pruski. Remote detection of mental workload changes using cardiac parameters assessed with a low-cost webcam. *Computers in Biology and Medicine*, 53(C):154–163, oct 2014.

[6] Coni˜nunicated By, John Platt, Simon Haykin, Anthony J Bell, and Terrence J Sejnowski. An Information-Maximization Approach to Blind Separation and Blind Deconvolution.

[7] Lung-Sang Chan, Giselle T. Y. Cheung, Ian J. Lauder, and Cyrus R. Kumana. Screening for Fever by Remote-sensing Infrared Thermographic Camera. *Journal of Travel Medicine*, 11(5):273–279, mar 2006.

[8] Ke-Lin Du and M. N. S. Swamy. Independent Component Analysis. In *Neural Networks and Statistical Learning*, pages 419–450. Springer London, London, 2014.

[9] C. Y. N. Dwith, Pejhman Ghassemi, Joshua Pfefer, Jon Casamento, and Quanzeng Wang. Multi-modality image registration for effective thermographic fever screening. page 100570S. International Society for Optics and Photonics, feb 2017.

[10] Bernd Fischer and Jan Modersitzki. A unified approach to fast image registration and a new curvature based registration technique. *Linear Algebra and its Applications*, 380:107–124, mar 2004.

[11] Xuejun Gu, Hubert Pan, Yun Liang, Richard Castillo, Deshan Yang, Dongju Choi, Edward Castillo, Amitava Majumdar, Thomas Guerrero, and Steve B Jiang. Implementation and evaluation of various demons deformable image registration algorithms on a GPU. *Physics in Medicine and Biology*, 55(1):207–219, jan 2010.

[12] Alastair D Hay, Tim J Peters, Andrew Wilson, and Tom Fahey. The use of infrared thermometry for the detection of fever. *British Journal of General Practice*, 54(503), 2004.

[13] Derek L. G. Hill, David J. Hawkes, Neil A. Harrison, and Cliff F. Ruff. A strategy for automated multimodality image registration incorporating anatomical knowledge and imager characteristics. In *Information Processing in Medical Imaging*, pages 182–196. Springer-Verlag, Berlin/Heidelberg, 1993.

[14] Berthold K P Horn and Brian G Schunck. Determining Optical Flow.

[15] Kenneth Humphreys, Tomas Ward, and Charles Markham. Noncontact simultaneous dual wavelength photoplethysmography: A further step toward noncontact pulse oximetry. 2007.

[16] Aapo Hyvärinen, Aapo Hyvärinen, and Erkki Oja. A Fast Fixed-Point Algorithm for Independent Component Analysis. *NEURAL COMPUTATION*, 9:1483—-1492, 1997.

[17] Jin Jin Fei and I. Pavlidis. Thermistor at a Distance: Unobtrusive Measurement of Breathing. *IEEE Transactions on Biomedical Engineering*, 57(4):988–998, apr 2010.

[18] E Kee and E Ng. Fever Mass Screening Tool for Infectious Diseases Outbreak. In *Medical Infrared Imaging*, pages 16–1–16–19. CRC Press, jul 2007.

[19] Thomas M Lehmann, Claudia Gönner, and Klaus Spitzer. Survey: Interpolation Methods in Medical Image Processing. *IEEE TRANSACTIONS ON MEDICAL IMAGING*, 18(11), 1999.

[20] Hava Lester and Simon R. Arridge. A survey of hierarchical non-linear medical image registration. *Pattern Recognition*, 32(1):129–149, jan 1999.

[21] Jiayi Ma, Ji Zhao, Yong Ma, and Jinwen Tian. Non-rigid visible and infrared face registration via regularized Gaussian fields criterion. *Pattern Recognition*, 48(3):772–784, 2015.

[22] Jiayi Ma, Ji Zhao, Yong Ma, and Jinwen Tian. Non-rigid visible and infrared face registration via regularized Gaussian fields criterion. *Pattern Recognition*, 48(3):772–784, 2015.

[23] J B Antoine Maintz and Max A Viergever. A survey of medical image registration. *Medical Image Analysis*, 2(1):1–36, 1998.

[24] David Mattes, David R. Haynor, Hubert Vesselle, Thomas K. Lewellyn, and William Eubank. <title>Nonrigid multimodality image registration</title>. pages 1609–1620, jul 2001.

[25] Nadica Miljkovic, Vladimir Matic, Sabine Van Huffel, and Mirjana B. Popovic. Independent Component Analysis (ICA) methods for neonatal EEG artifact extraction: Sensitivity to variation of artifact properties. In *10th Symposium on Neural Network Applications in Electrical Engineering*, pages 19–21. IEEE, sep 2010.

[26] Jan Modersitzki. *Numerical Methods for Image Registration*. Oxford University Press, dec 2003.

[27] Yu B Monakhova, S P Mushtakova, S S Kolesnikova, and S A Astakhov. Chemometrics-assisted spectrophotometric method for simultaneous determination of vitamins in complex mixtures.

[28] Ganesh R. Naik. A comparison of ICA algorithms in surface EMG signal processing. *International Journal of Biomedical Engineering and Technology*, 6(4):363, 2011.

[29] Eddie Y.-K. Ng and Eddie Y.-K. Is thermal scanner losing its bite in mass screening of fever due to SARS? *Medical Physics*, 32(1):93–97, dec 2004.

[30] Eddie Y.K Ng, G.J.L Kawb, and W.M Chang. Analysis of IR thermal imager for mass blind fever screening. *Microvascular Research*, 68(2):104–109, 2004.

[31] Jorge. Nocedal and Stephen J. Wright. *Numerical optimization*. Springer, 2006.

[32] A. K. Noulas and B. J. A. Kröse. EM detection of common origin of multi-modal cues. In *Proceedings of the 8th international conference on Multimodal interfaces - ICMI '06*, page 201, New York, New York, USA, 2006. ACM Press.

[33] Nowak, Magdalena Lewandowska, Jacek Rumiński, Tomasz Kocejko, and Jędrzej. Measuring pulse rate with a webcam; A non-contact method for evaluating cardiac activity. *2011 Federated Conference on Computer Science and Information Systems (FedCSIS)*, (ISBN 978-83-60810-22-4):405–410, 2011.

[34] M Pettersson and A Strandell. [Temperature measurements in health care–a question of quality assurance]. *Lakartidningen*, 97(37):4050, sep 2000.

[35] Josien P W Pluim, J B Antoine Maintz, and Max A Viergever. Mutual-Information-Based Registration of Medical Images: A Survey. *IEEE TRANSACTIONS ON MEDICAL IMAGING*, 22(8), 2003.

[36] Ming-Zher Poh, Daniel J. McDuff, and Rosalind W. Picard. Non-contact, automated cardiac pulse measurements using video imaging and blind source separation. *Optics Express*, 18(10):10762, may 2010.

[37] Ming-Zher Poh, Daniel J Mcduff, and Rosalind W Picard. Advancements in Noncontact, Multiparameter Physiological Measurements Using a Webcam. *IEEE TRANSACTIONS ON BIOMEDICAL ENGINEERING*, 58(1), 2011.

[38] Ming-Zher Poh, Daniel J McDuff, Rosalind W Picard, S Cook, M Togni, M C Schaub, P Wenaweser, and O M Hess. Non-contact, automated cardiac pulse measurements using video imaging and blind source separation.

[39] Ming-Zher Poh, Nicholas C. Swenson, and Rosalind W. Picard. Motion-tolerant magnetic earring sensor and wireless earpiece for wearable photoplethysmography. *IEEE Transactions on Information Technology in Biomedicine*, 14(3):786–794, may 2010.

[40] E F J Ring. New standards for fever screening with thermal imaging systems. In *Infrared Imaging*. IOP Publishing, 2014.

[41] D.N. Rutledge and D. Jouan-Rimbaud Bouveresse. Independent Components Analysis with the JADE algorithm. *TrAC Trends in Analytical Chemistry*, 50:22–32, 2013.

[42] Christopher G Scully, Jinseok Lee, Joseph Meyer, Alexander M Gorbach, Domhnull Granquist-Fraser, Yitzhak Mendelson, and Ki H Chon. Physiological parameter monitoring from optical recordings with a mobile phone. *IEEE transactions on bio-medical engineering*, 59(2):303–6, feb 2012.

[43] J.-P. Thirion. Image matching as a diffusion process: an analogy with Maxwell's demons. *Medical Image Analysis*, 2(3):243–260, sep 1998.

[44] Birgit K. van Staaij, Maroeska M. Rovers, Anne G. Schilder, and Arno W. Hoes. Accuracy and feasibility of daily infrared tympanic membrane temperature measurements in the identification of fever in children. *International Journal of Pediatric Otorhinolaryngology*, 67(10):1091–1097, oct 2003.

[45] Wim Verkruysse, Lars O Svaasand, and J Stuart Nelson. Remote plethysmographic imaging using ambient light. *Optics Express*, 16(26):21434, dec 2008.

[46] P. Viola and M. Jones. Rapid object detection using a boosted cascade of simple features. In *Proceedings of the 2001 IEEE Computer Society Conference on Computer Vision and Pattern Recognition. CVPR 2001*, volume 1, pages I–511–I–518. IEEE Comput. Soc.

[47] F. P. Wieringa, F. Mastik, and A. F. W. van der Steen. Contactless Multiple Wavelength Photoplethysmographic Imaging: A First Step Toward SpO2 Camera Technology. *Annals of Biomedical Engineering*, 33(8):1034–1041, aug 2005.

[48] John C. Woods, Roger P.; Cherry, Simon R.; Mazziotta. Rapid Automated Algorithm for Aligning and Reslicing PET Ima... : Journal of Computer Assisted Tomography. *Journal of Computer Assisted Tomography*, 1992.

[49] W G Zijlstra, A Buursma, and W P Meeuwsen-van der Roest. Absorption spectra of human fetal and adult oxyhemoglobin, de-oxyhemoglobin, carboxyhemoglobin, and methemoglobin. *Clinical Chemistry*, 37(9), 1991.

[50] Barbara Zitová and Jan Flusser. Image registration methods: a survey.